UNIVERSITÀ DEGLI STUDI DI CATANIA
Dipartimento di Ingegneria Elettrica Elettronica e Informatica

Ph.D. Course in Systems Engineering (XXVIII cycle)
Ph.D. Thesis

MODELING SOLAR RADIATION AND WIND SPEED TIME SERIES FOR RENEWABLE ENERGY APPLICATIONS

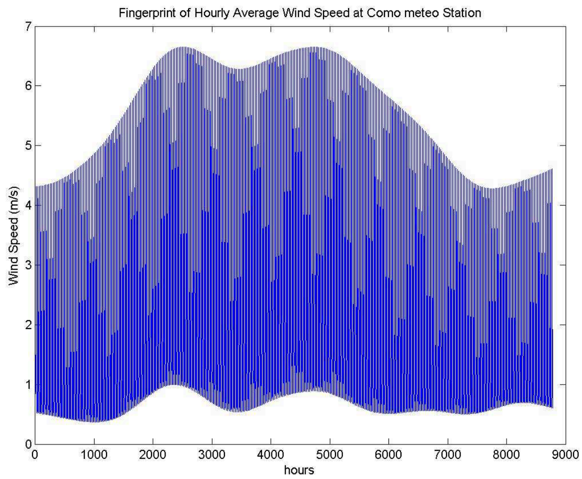

Silvia Nunnari

Tutors: Prof. Luigi Fortuna
Prof. Giorgio Guariso
Coordinator: Prof. Luigi Fortuna

To my parents

Life is a mystery, discover it.
Mother Teresa

The problem of predicting weather variables, such as solar radiation and wind speed, is of great interest for integrating renewable energies plants, into the electric grid. Indeed, since renewable energy sources are intermittent in nature, predicting future values is important to allow the grid to dispatching generators, in order to satisfy the demand. There are essentially two ways to address the issue of weather variables prediction. One is by using Numerical Weather Forecasting (NWF) models, which are reliable, but also quite complex and requires real time information, usually available from Meteorological Agencies only. Furthermore, very powerful computers are required to solve the differential equations involved. The other kinds of methods are represented by the so-called statistical modeling approaches, which are based on the use of past data recorded at the site of interest. These latter kinds of methods, compared to the former ones, require less computational efforts, but are appropriate only for short time horizons.
This PhD Thesis was devoted to study short-term prediction models for solar radiation and wind speed time series and assessing their performance in the range $[1, 24]$ hours.
It was also studied the predictability of the daily average values, which for obvious reasons, is much more difficult than that of predicting the hourly averages. To mitigate, as far as possible, the difficulties, the prediction was reformulated in terms of a classification problem. In such a way, instead of predicting 1-day ahead the average value, the target was to predict the class. In this framework, of course, the prediction is as far difficult as large is the number of considered classes. The accuracy of 1-day ahead prediction models of the wind speed class was studied, for various frameworks.

The structure of the Thesis is the following. Some background about solar radiation and wind speed energy is presented in Chap. 1. Analysis of solar radiation and wind speed time series, recorded in different areas are presented in Chap. 2 and 3, respectively. Some literature references dealing with techniques for modeling wind speed and solar radiation time series are given in Chap. 4, focusing essentially on NAR (Nonlinear Auto Regressive) and EPS (Embedded Phase Space) models, since are the ones considered in this work. Results obtained by modeling solar radiation and wind speed time series are reported in Chap. 5 and 6 respectively. Clustering approaches of daily pattern of solar radiation and wind speed time series are given in Chap 7 and 8, respectively, while concluding remarks are sketched in Chap. 9.

Contents

1

Background

Several form of alternative sources of energy are present in nature almost in unlimited quantities, referred to as *renewable*, since are continuously regenerated. The main renewable sources are based on solar energy, on thermal energy contained in the Earth interior and on gravitational energy. From the Sun naturally derives accumulations of water to produce hydroelectric power, wind for aeolic turbine generators, electric energy by photovoltaics plants and solar thermal. Furthermore from the photosynthesis process it is possible to derive energy from biomass. The following sections focuses essentially on solar radiation and wind speed energy, since are the ones considered in this work. Most of information reported in this chapter refers to [1] and [2].

1.1 Energy from the Sun

The Sun is certainly the main source of renewable energy. Just to have an idea it is possible to say that the Sun delivers towards the surface of the terrestrial hemisphere exposed a power exceeding 50

thousand Tera Watt which is about 10 thousand times the energy used all over the world [1]. A part of this energy reaches the outer part of the Earths atmosphere with an average irradiance of about 1367 W/m^2, a value which varies as a function of the Earth-to-Sun distance and of the solar activity (sunspots). The problem of estimating the average hourly global solar radiation $I(h, d)$, for any hour h of a day d of the year, at any site, has been addressed in literature by several authors such as [3]. It depends on a quite large number of parameters which, roughly speaking, can be summarized as follows: the distance from the sun, the duration of the daily sunlight period, the inclinations of solar rays to the horizon, the transparency of the atmosphere towards heat radiation and the output of solar radiation. Some of these factors are connected with mechanical parameters which describes the revolution of Earth around the Sun and on the Earth spinning about itself. Others factors depend on the properties of the atmosphere and are stochastic in nature, such as the cloud cover features (size, speed and number) and the degree of pollution.
The average annual irradance in European Countries is shown in Figure 1.1. In particular in Italy the average annual irradiance varies from 3.6 KWh/m^2 a day of the Po Valley to the 4.7 KWh/m^2 a day in the South and Centre and to the 5.4 KWh/m^2 a day of Sicily. When passing through the atmosphere, the solar radiation decreases in intensity because it is partially reflected and absorbed (above all by the water vapor and by the other atmospheric gases). The radiation which passes through is partially diffused by the air and by the solid particles suspended in the air, as shown in Figure 1.2. Therefore the radiation falling on a

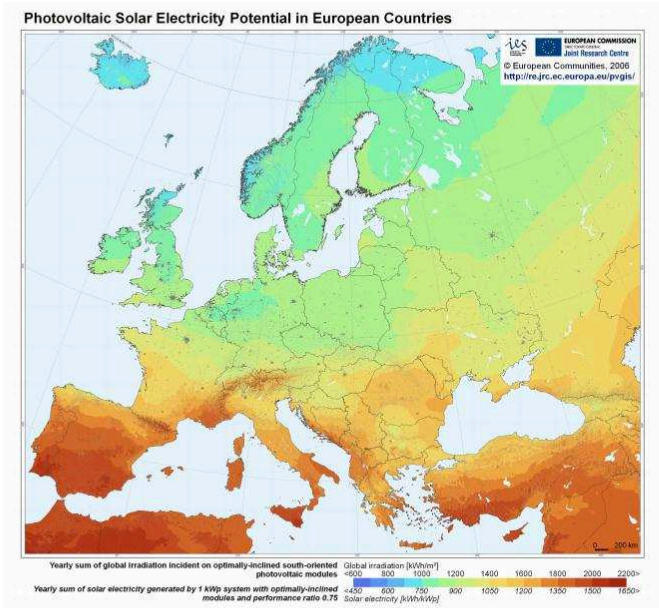

Fig. 1.1. Solar Radiation in Europe

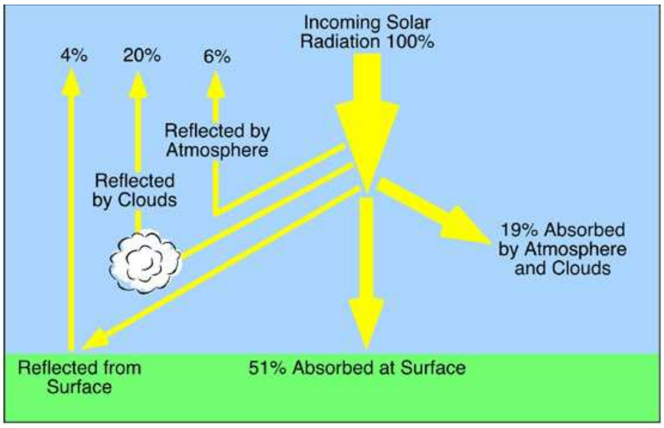

Fig. 1.2. Energy flow from the Sun.

horizontal surface is constituted by a direct radiation, associated to the direct irradiance on the surface, by a diffuse radiation which strikes the surface from the whole sky and not from a specific part of it and by a radiation reflected on a given surface by the ground and by the surrounding environment. In winter the sky is overcast and the diffuse component is greater than the direct one.

1.2 Energy from the Wind

The Earth continuously releases into the atmosphere the heat received by the sun, but unevenly. In the areas where less heat is released (cool air zones) the pressure of atmospheric gases increases, whereas where more heat is released, air warms up and gas pressure decreases. As a consequence, a macro-circulation due to the convective motions is created as shown in Figure 1.3. Air masses get warm, reduce their density and rise, thus drawing cooler air flowing over the earth surface. This motion of warm and cool air masses generates high pressure and low pressure areas permanently present in the atmosphere and also influenced by the rotation of the earth. Since the atmosphere tends to constantly re-establish the pressure balance, the air moves from the areas where the pressure is higher towards those where it is lower; therefore, wind is the movement of an air mass, more or less quick, between zones at different pressure. The greater the pressure difference, the quicker the air flow and consequently the stronger the wind. In reality, the wind does not blow in the direction joining the center of the high pressure with that of the low pressure, but in the northern hemi-

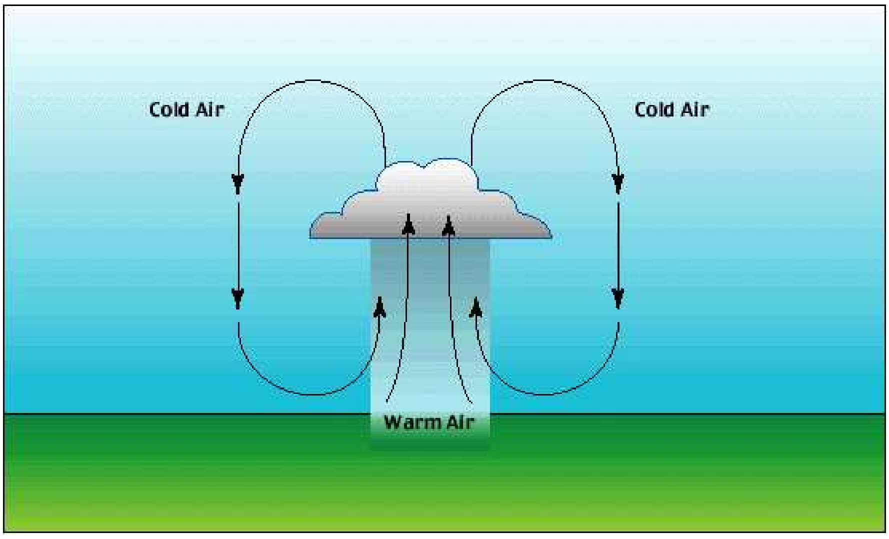

Fig. 1.3. Air mass circulation due to Solar Radiation.

sphere it veers to the right, circulating around the high pressure centers with clockwise rotation and around the low pressure ones in the opposite direction. In the practice, who keeps his back to the wind has on his left the low pressure area **B** and on his right the high pressure area **A**, as shown in Figure 1.4. In the southern hemisphere the opposite occurs.

On a large scale, at different latitudes, a circulation of air masses can be noticed, which is cyclically influenced by the seasons. On a smaller scale, there is a different heating between the dry land and the water masses, with the consequent formation of the daily sea and earth breezes. The profile and unevenness of the surface of the dry land or of the sea deeply affect the wind and its local characteristics; in fact the wind blows with higher intensity on large and flat surfaces, such as the sea: this represents the main element of

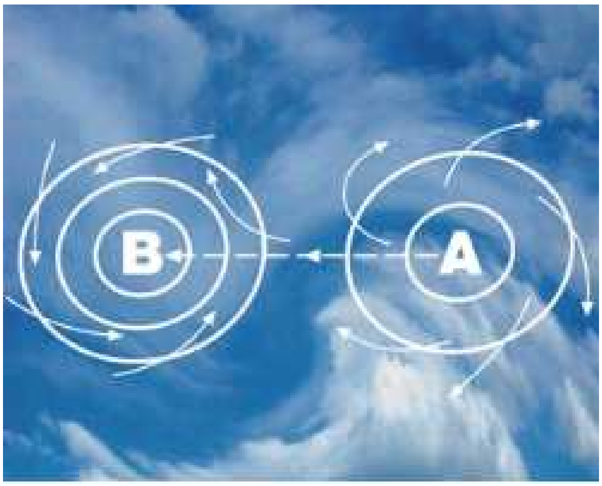

Fig. 1.4. Wind rotation around high and low pressure centers.

interest for wind plants on-and off shore. Moreover, the wind gets stronger on the top of the rises or in the valleys oriented parallel to the direction of the dominant wind, whereas it slows down on uneven surfaces, such as towns or forests, and its speed with respect to the height above ground is influenced by the conditions of atmospheric stability.

The average wind speed in Italy, measured at 25 m a.s.l., ranges from $6-7$ m/s from the South Eastern to the 3 m/s of the Northern part of Italy, but the largest areas are featured by $4-5$ and $5-6$. m/s, as shown in Figure 1.5. In order to exploit wind energy, it is very important to take into account the strong speed variations between different places: sites separated by few kilometers may be subject to very different wind conditions and have different implication for the installation purposes of wind turbines. The strength of the wind changes on a daily, hour or minute scale, according

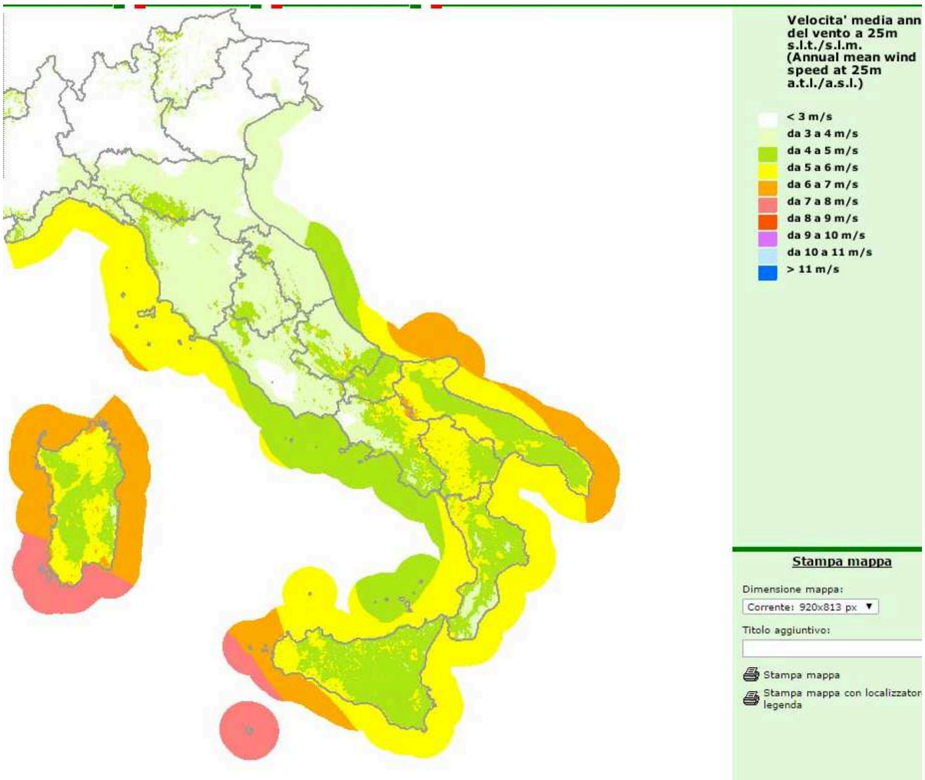

Fig. 1.5. Average wind speed map in m/s in Italy as results from http://atlanteeolico.rse-web.it/viewer.htm.

to the weather conditions. Moreover, the direction and intensity of the wind fluctuate rapidly around the average value: it is the turbulence, which represents an important characteristic of wind since it causes fluctuations of the strength exerted on the blades of the turbines, thus increasing wear and tear and reducing their mean life. On complex terrain, the turbulence level may vary between 15% and 20%, whereas in open sea this value can be comprised in the range from 10% to 14%. Variability and uncertainty of winds represent the main disadvantages of the electrical energy derived from the wind source. In fact, as far as the amount of power produced by the wind plant is small in comparison with the size of the grid to which it is connected, the variability of energy production from wind source does not destabilize the grid itself and can be considered as a change in the demand for conventional generators. Instead, in some countries, large-size wind plants are being considered, prevailingly offshore groups of turbines. Such wind farms shall have a power of hundreds of MW, equivalent to that of conventional plants, and therefore their variability cannot be considered as a noise on the demand of energy and becomes important to foresee their energy production in advance.

1.3 Conclusions

The aim of this section was to describe the essential background of the two forms of renewable energy considered in this work. From this description, although not exhaustive, it should be possible to understanding that the solar and wind energies are governed by spatially distributed phenomena. Indeed, solar radiation is greatly influenced by the clouds cover features (size, speed and number) and to others variables including atmospheric transmittance, sky turbidity and pollution level. Similarly wind speed depends by pressure differences that occur in various areas but, it is strongly influenced also by quite complex phenomena occurring into the atmospheric boundary layer, i.e. the lower part of the atmosphere. Nevertheless, in this work all such phenomena will be ignored, since our modeling approach is based on taking into account time series recorded at the ground, in the site of interest only. Indeed this is normally the situation in which a plant manager operates, unless he wants to use more complex meteorological information, usually available from Meteorological Agencies only. The goal is that of assessing to what extent short term predictions of solar radiation and wind speed are reliable based on past data recorded at the site of interest only.

2

Analysis of Solar Radiation Time Series

The topic of solar radiation time series analysis has been addressed in literature by various authors such as [4], [5] and [6]. Nevertheless, as the results available in the literature are sometimes fragmented, in this chapter I will try to provide a picture as comprehensive as possible of properties of this kind of time series. For the purposes of this analysis data set recorded in various geographic locations were considered in order to preserve the generality of the results. Analysis performed refer to aspects such as stationarity, power spectrum, autocorrelation, fractal and multifractal properties and features such as the embedding state space dimension and the Lyapunov spectrum.
Solar radiation time series, at various time scales are shown in Figure (2.1). According with the basic knowledge about solar radiation, the Figure confirms that the considered time series are fluctuating at any time scale. In the Figure the same time series is shown at hourly, daily, monthly and yearly time scales. Fluctuations observed in solar radiation time series is a feature shared with other meteorological time series, such as wind speed. These fluctuations are

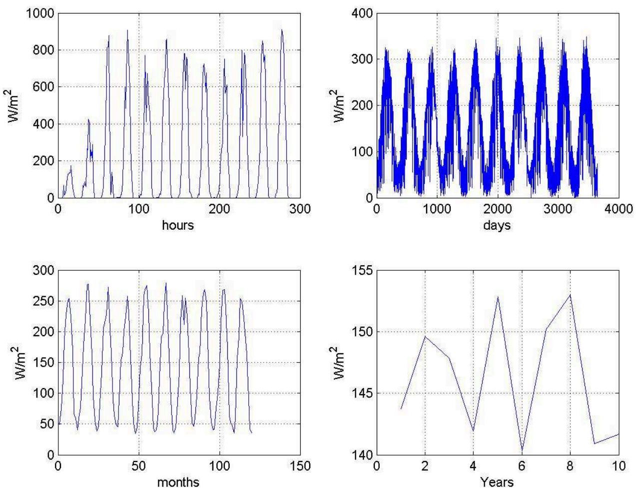

Fig. 2.1. Solar Radiation time series recorded at Lambrate

superimposed with deterministic variation due to the Earth spinning around itself and to the revolution of Earth around the Sun. The Earth spinning determines the typical bell shape curves that are visible at hourly scale while the revolution around the Sun determines and the fluctuations that are visible at monthly scales. However fluctuations occurs also from year to year, as shown in lower rightmost sub Figure (2.1).

2.1 Stationarity Analysis

One of the early questions that one would like to know is if solar radiation time series are stationary or not. This is not a simple task. Usually, available tests are based on the search for existent of a *unit root*, such as the Dicky-Fuller, the Phillips-Perron tests and the Kwiatkowski-Phillips-Schmidt-Shin test or the Variance Ratio test which is based on assessing if time series are random walks. The application of all these tests indicate that the null-hypothesis, i.e. that the considered time series are non stationary, is false. I have also searched for nonstationary evidences in solar radiation time series by using recurrent plots as shown in Figure (2.2). The Fig-

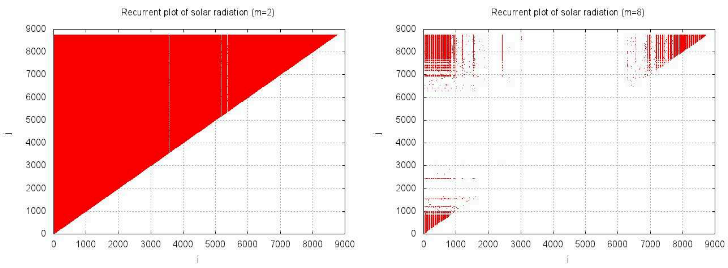

(a) (b)

Fig. 2.2. Recurrent plots of Solar Radiation for two different embedding dimensions. (a) m=2 (b) m=8

ure shows recurrent plots for two different embedding dimensions ($m = 2$) and ($m = 8$). Since we know that in an ergodic situation, the dots of a recurrent plot should cover the plane uniformly on average, whereas non-stationarity expresses itself by an overall tendency of dots to be close to the diagonal, we can say that there are not evidences to conclude that solar radiation time series are non stationary, at least for time interval of 10 years, as in the case study here described.

2.2 Space-time plots

The space-time plot computed from hourly average solar radiation time series, computed for $m = 12$ is shown in Figure (2.3). The

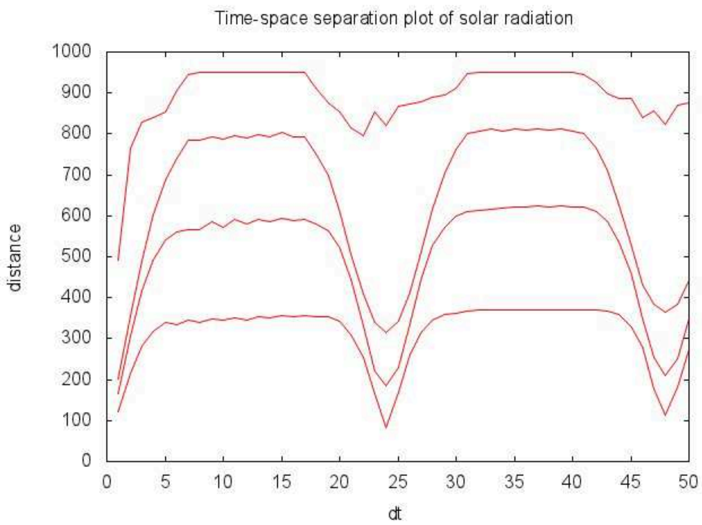

Fig. 2.3. pace-time separation plot of Solar Radiation (m=12, d=2).

Figure shows lines of constant probability density of a point to be an neighbor of the current point if its temporal distance is δt. Probability densities are from 0.25 to 1 with increments of 0.25 from bottom to top. Clear correlations are visible. It is possible to see that for $\delta t \leq 6$ there space variation as larger as allowed. This results can be interpreted in the sense that 6 hours can be assumed as the temporal distance between independent samples, as further confirmed by autocorrelation analysis performed in the next section. Furthermore, the obtained value can be assumed as a good candidate for the delay parameter τ in the embedding phase-space modeling approach, that will be considered in Chap. 5 for modeling purposes.

2.3 Autocorrelation and Mutual Information

The autocorrelation functions computed for hourly and daily average solar radiation time series are reported in Figure (2.4). As

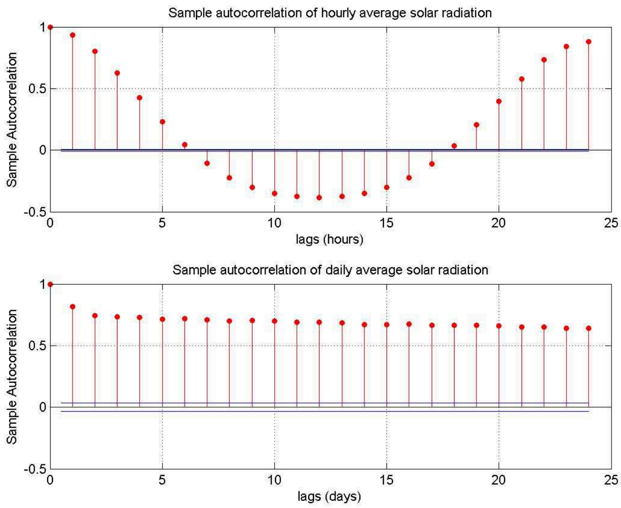

Fig. 2.4. Autocorrelation of hourly and daily average solar radiation time series at Lambrate.

it is possible to see at hourly scale the autocorrelation function is strongly periodic with period 24 hours, as it was expected, due to the marked daily component which features solar radiation time series (see Figure (2.1) at hourly scale). Furthermore, the autocor-

relation function computed at hourly scale decays at values lower than 0.37 (the so-called correlation time τ_c, in about 5 lags (hours), which is close to the $\delta t \simeq 6$, estimated from the time-space plot.
At daily scale the autocorrelation reaches a minimum after a few (say 2 lags), but how it is possible to appreciate it decays very slowly.
However it is to bearing in mind that autocorrelation is a linear feature of time series. Since it is highly probable that solar radiation is generated by non linear processes, it is more appropriately to estimate also the mutual information, as shown in Figure (2.5).
The Figure, in essence, confirms that at hourly scale the correlation

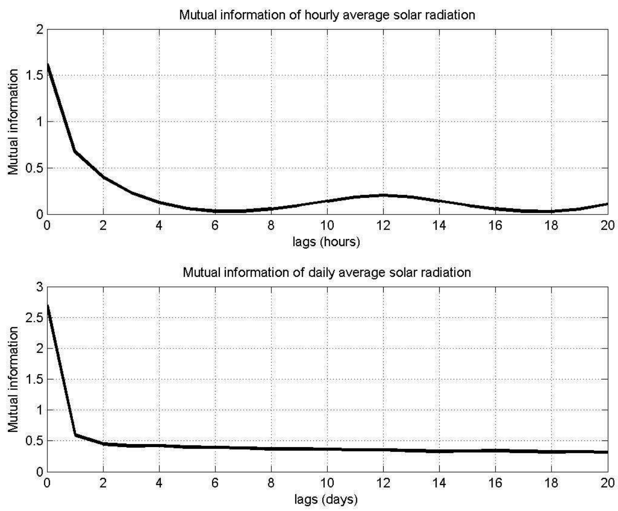

Fig. 2.5. Autocorrelation of hourly and daily average solar radiation time series at Lambrate.

time τ_c, is about $5 \div 6$ lags at hourly scale and $1 \div 2$ lags at daily scale. This is a first assessment of the time horizon within which it is possible to make reliable predictions by using autoregressive models. However in this work, I have studied the prediction error in the overall range $h \in [1, 24]$ for hourly average time series, as it will be described in Chap. 5.

2.4 Power Spectra

The power spectra of hourly and daily solar radiation time series are shown in Figure (2.6). It is possible to observe that at hourly scale

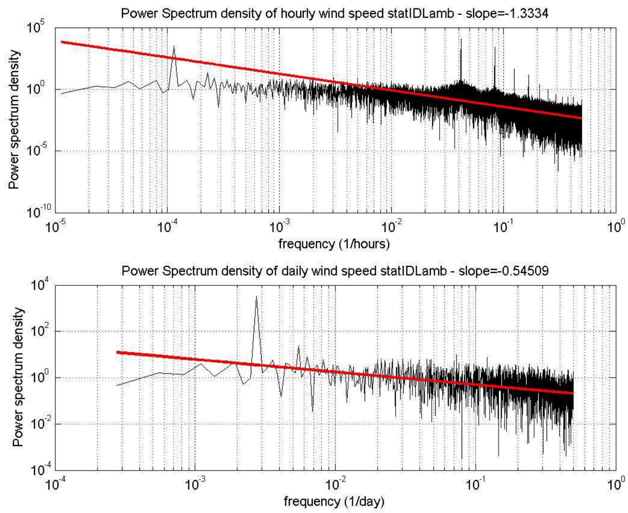

Fig. 2.6. Power spectrum densities of hourly and daily average solar radiation time series at Lambrate.

there are marked components with periods: $T_1 = 1/0.0001143 \simeq 8748$ hours $\simeq 1$ year, $T_2 = 1/0.04167 \simeq 24$ hours. The others com-

ponents of the spectrum computed at hourly scale corresponding to periods of 12 hours, 6 hours etc, are well known effects of the considered Fast Fourier Transform (FFT) computing algorithm. At daily scale only one marked component is evident, corresponding to a period of $T_3 = 1/0.002743 \simeq 365$ days, i.e. 1 year.
Further, Figure (2.6) shows that the slope of the power spectrum is about -1.33 at hourly scale and -0.54 at daily scale. The difference among these slopes can be easily explained bearing in mind that daily average solar radiation time series are less autocorrelated then the corresponding hourly average time series, and thus more similar to a white noise. Based on slopes of power spectra, it is possible to say that solar radiation time series belongs to the ubiquitous $1/f$ noise.

2.5 Hurst Exponent and Fractal dimension

The Hurst exponents and the fractal dimensions of hourly average time series computed for ten years at one of the considered recording stations are shown in Figure (2.7). The Hurst exponent was computed by using the R/S algorithm while the fractal dimension was computed by using the boxcounting algorithm. It is possible to see that, H and D, computed on windows of 1 year, gives on average $H = 0.75$ and $D = 1.3$. Thus the Hurst exponent is close to the range 0.73 ± 0.09 observed for several natural time series. Furthermore it is possible observe that the theoretical relation $H = 2 - D$ approximately holds.

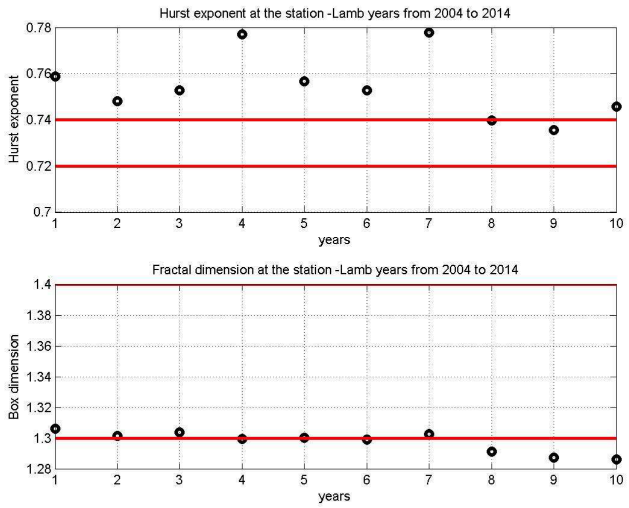

Fig. 2.7. Hurst exponent and Fractal dimension of hourly average solar radiation time series at Lambrate.

2.6 Multifractal spectrum of solar radiation

Results of multifractal analysis performed on solar radiation time series is shown in Figure (2.8). In more detail, the left-upper sub Figure shows, in a log-log scale, the scaling function F_q versus the scale (from 64 to 4096 samples), for various values of the q (the local order of the local fluctuation exponent). Here it is to bearing in mind that negative q-order, e.g. ($q = -5$), amplifies the segments in the multifractal time series with extreme small fluctuations, whereas positive q-order e.g. ($q = 5$), amplifies the segments with extreme large fluctuations. The midpoint $q = 0$ is neutral to influence of segments with small and large fluctuation. Finally observe that the slope of the regression lines, is the Hurst exponent

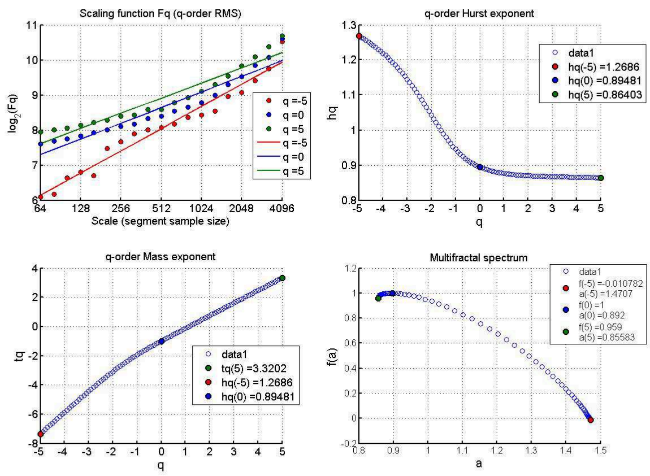

Fig. 2.8. Multifractal spectrum at Lambrate (Milan) (hourly average from 2012 to 2014)

H corresponding to the considered q, also referred to as the generalized Hurst exponent $H(q)$. Here it is to be stressed that while a mono-fractal time series exhibits regression lines with the same slope for various q, this is not the case of solar radiation time series. Indeed, in the considered example (see the top rightmost sub Figure (2.8)) the q-order Hurst exponent varies from 1.26 to 0.84 when q varies from -5 to 5. In more detail, it should be stressed that for $q = 2$ the generalized hurst exponent gives the Hurst exponent on the ordinary (i.e. mono fractal) fluctuation analysis. Such a value is usually a little different from the Hurst exponent obtained by using the R/S algorithm considered in section 2.5. The so-called mass exponent τ_q versus q, which is related to the q-order Hurst exponent, $H(q)$, by expression (2.1)

$$\tau(q) = qH(q) - 1 \tag{2.1}$$

is shown in the leftmost bottom sub Figure (2.8). This curve, in case of a mono-fractal time series is exactly a straight line, since in this case the q-order Hurst exponent is independent on q. As it is possible to observe this is not the case of solar radiation, since in this case we have a curve with the concavity facing down. Finally the multi fractal spectrum (also referred to as singularity spectrum) is shown in the lower rightmost sub Figure (2.8). As in general the multi fractal spectrum assume an asymmetric bell shape with the maximum obtained for q = 0, in the example shown in Figure the spectrum is left truncated. This simply means that while large fluctuation scales within a limited range of Lipshitz-Holder exponents in the range ($\alpha \in [0.8, 0.9]$), the small fluctuation scales following a winder range of exponents ($\alpha \in [0.9, 1.5]$). This feature, seems to be shared by solar radiation time series recorded in different areas, as shown in Figure (2.9.b). In the Figure the singularity spectrum of solar radiation at five stations is shown. Four of the stations, referred to as Lamb (Lambrate, Milano), Casa (Casatenovo, Lecco), Stez (Stezzano, Bergamo) and Como (Como), respectively are located in Lombardia while Aber is located at Aberdeen (Ohio,USA). While the four recording stations located in Lombardia are all in the Po Valley at low altitude, Aberdeen is located in USA at 1433 m a.s.l. Probably the different altitude of the recording station may explain why singularity spectrum at Aberdeen is less wide, i.e. more close to be monofractal, with respect to the others.

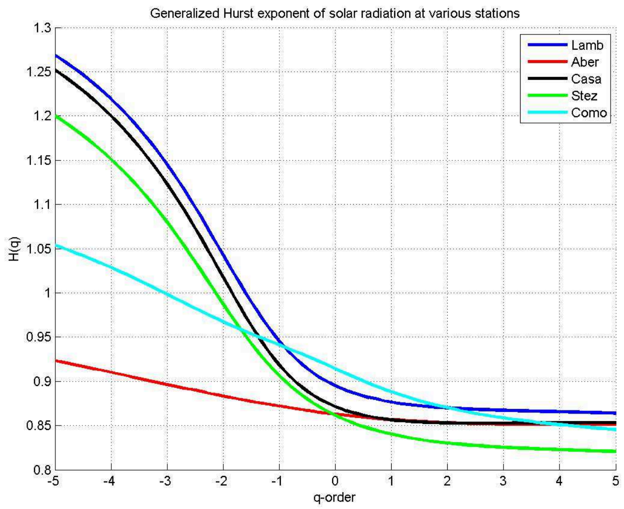

(a)

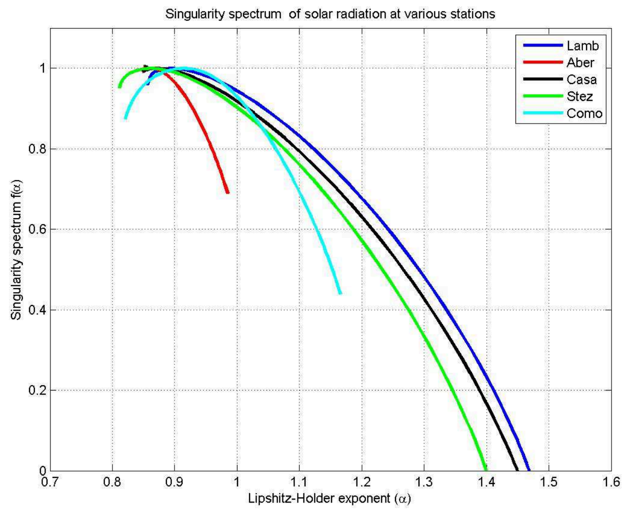

(b)

Fig. 2.9. Generalized Hurst exponent and singularity spectrum at four solar radiation recording stations (a) Generalized Hurst (b) Multifractal Spectrum.

2.7 Estimation of the embedding dimension

In order to determine the embedding dimension m of solar radiation time series, I have evaluated the fraction of false nearest neighbors versus m, as shown in Figure (2.10). The Figure shows that the

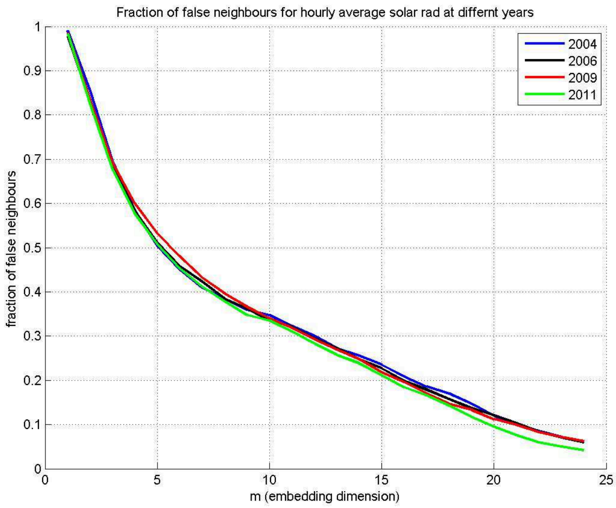

Fig. 2.10. Fraction of false nearest neighbors of solar radiation at Lambrate at different years-

fraction of false nearest neighbors decays very slowly with the embedding dimension, without reaching the zero value in the range $m \in [1, 30]$. This results could means that the supposed non-linear dynamical system, underlaying the solar radiation process in not low dimensional; however, it could also be interpreted as the effect of noise in the considered time series.

2.8 Maximal Lyapunov exponent

Lyapunov exponents are an important means of quantification for unstable systems. They are however difficult to estimate from time series. Unless the underlying dynamical system is low dimensional and high quality data are available, it is non recommended to compute the full spectrum and at most it is recommended try to compute the maximal exponent only. To this purpose, I have considered the lyapk function which is part of the TISEAN package. Results obtained by using this algorithm on hourly average time series recorded at different stations indicate the existence of positive maximal exponents in the range $[0.6, 1]$.

2.9 Conclusions

Analysis presented in this chapter, performed on both hourly and daily average solar radiation time series allow to draw some conclusions about their nature. Stationary analysis, carried out by different approaches, has not pointed out evidences that they are nonstationary, at least for time intervals of ten years, which is the largest considered in this study. The power spectrum analysis showed, in addition to the obvious presence of seasonal (mainly the daily and yearly) components, also that the slopes of the solar radiation time series power spectra are in the range $[0.5, 1.5]$, which, according with claims existing in literature, means that solar radiation time series belong to the wide class of $1/f$ noise. Correlation analysis, carried out by using linear and non linear approaches, pointed out that solar radiation time series exhibits a correlation time of about

$\tau_c = 5$ lags at hourly time scale and of about $\tau_c = 1$ lag at daily scale, which means that prediction models, based on autocorrelation only, have limited chances to be reliable, unless that for very short horizons. Fractal analysis pointed out that these kind of time series are fractal exhibiting, on average, fractal dimension $D = 1.3$ and Hurst exponent of $H = 0.75$. Furthermore, the Multi-Fractal Detrended Fluctuation Analysis (MFDFA) has pointed out that solar radiation time series are multi-fractal, exhibiting singularity spectra, computed for different recording stations and geographic areas, that are usually left-truncated, which means that while large fluctuation scales within a limited range of Lipshitz-Holder exponents ($\alpha \in [0.8, 0.9]$), the small fluctuation scales following a wider range of exponents ($\alpha \in [0.9, 1.5]$). Analysis carried out in order to see if there are evidences of deterministic chaos give controversial results. Indeed, the search for an embedding dimension pointed out that there is still a limited (i.e. ≤ 0.1) fraction of false nearest neighbors at high, dimension (e.g. $m = 24$). This results can be explained in different ways: the high embedding dimension is the effect of unavoidable noise in the time series or simply a low dimension chaotic attractor does not exists. On the other hand the computation of the maximal Lyapunov exponent has pointed out that there is at least a positive exponent in the range $[0.6, 1]$, thus meaning that a chaotic attractor could be hypothesized. In conclusion, since as well-known the computation of Lyapunov exponents from time series is quite difficult, at the present stage of this research, it is possible to affirm that while there are enough evidences to say that solar radiation time series belong to the large class of multifractal $1/f$ noises, there are not enough evidences to assess that a low dimensional chaotic attractor underlies the considered solar radiation time series.

3

Analysis of Wind Speed Time Series

The purpose of this chapter is to analyze a representative data set of wind speed time series recorded both in Italy and USA. The considered recording stations in Italy are mainly located in Lombardia and were provided both by the Politecnico di Milano (Como Campus) and by the ARPA Lombardia (see `http://ita.arpalombardia.it/ita/index.asp`). The stations located in USA are a subset of the Western Wind Resource (WWR) Dataset, modeled in the framework of the Western Wind and Solar Integration Study (see `http://wind.nrel.gov/`). Original time series were available with different sampling time: 5 min for the Como Campus data set, 10 min, for the WWR data set and 1 hour for the ARPA Lombardia data set. Data of the Como Campus station was recorded from 2011 to 2013, while the WWR dataset was recorded from 2004 to 2006; finally, data of the ARPA Lombardia is in general available since 2004. As for solar radiation, analysis performed on wind speed time series was devoted to assess general features such as stationarity, power spectrum, autocorrelation and mutual information, fractal and multifractal features, as suggested

by [7]). Furthermore, some kind of analysis were performed in order to assess the hypothesis of low dimensional chaos in wind speed time series, as claimed by ([8]). Some of the ideas described in this section were proposed in [9].
Description in this Chapter starts showing (see Figure (3.1)) that wind speed, such as solar radiation, are fluctuating time series at any time scale. However, of course, this not automatically implies

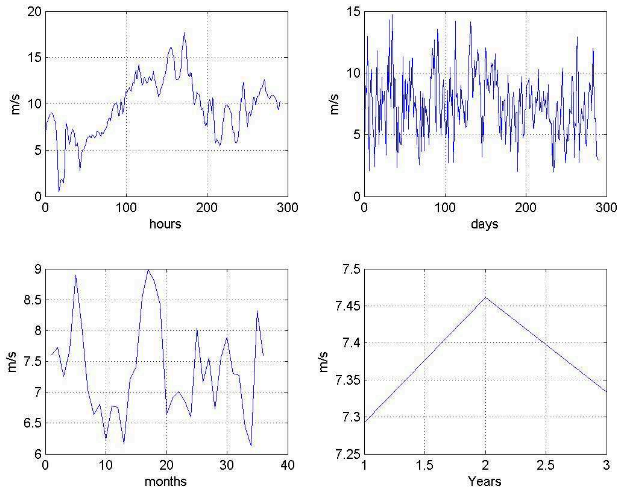

Fig. 3.1. Wind speed time series recorded at station ID2257

that they are nonstationary, as shown in the next section.

3.1 Stationary analysis

Stationary analysis was performed by various techniques, including the Augmented Dicky-Fuller (ADF) test, the Phillips-Pearson (PP) test, and the variance ratio (VR) test. All test rejected the null hypothesis, thus meaning that there are not enough evidences to assess that the considered time series are nonstationary, at least for time scale of three years. I tried also to assess stationarity by considering the recurrence plots. Recurrent plots of hourly wind speed time series, for different embedding dimensions, are shown in Figure (3.2). The uniform distribution of dots in the recurrent plots indicates that there are not particular structures that could be related with non stationarity, thus confirming achievement of the ADF, PP and VR tests.

3.2 Autocorrelation and Mutual Information

The power spectrum and autocorrelation function computed on hourly average wind speed time series are reported in Figure (3.3). As it is possible to see at hourly scale the autocorrelation function exhibits a slow decaying behavior, which is typical of $1/f$ noise. Indeed autocorrelation at daily scale decays at meaningless levels in about 3 lags. Autocorrelation of wind speed time series was also estimated in terms of mutual information, as shown in Figure (3.4). The Figure, in essence, confirms that the correlation time τ_c is about 6 lags at hourly scale and 2 lags at daily scale. This is a first assessment of the time horizon within which it is possible to make reliable predictions by using autoregressive models. However, in this work, I have studied the prediction error in the overall range $h \in [1, 24]$.

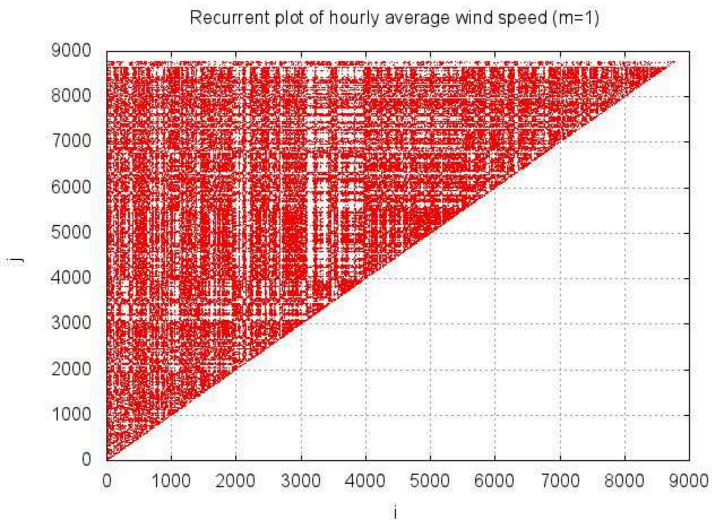

(a)

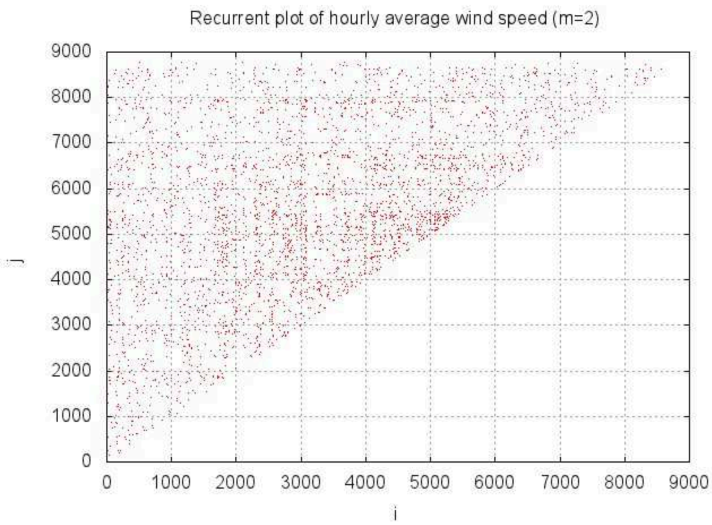

(b)

Fig. 3.2. Recurrence plots of hourly wind speed at station ID 2257 during 2004 for different embedding dimensions (a) m=1 (b) m=2

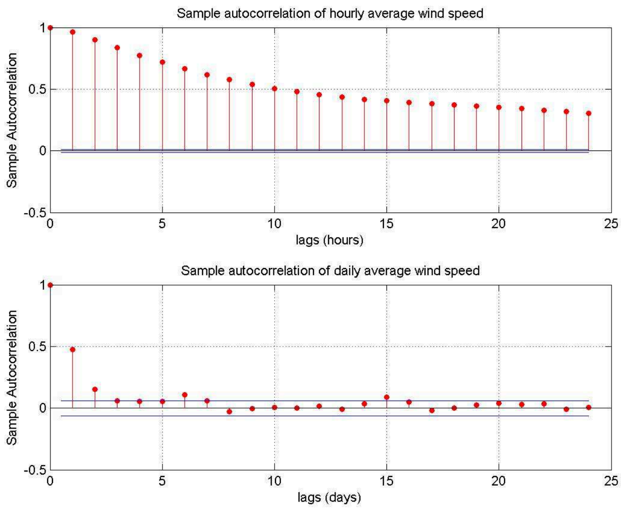

Fig. 3.3. Autocorrelation of hourly and daily average solar radiation time series at the ID2257 station.

3.3 Power Spectra

Typical power spectra of hourly and daily average wind speed time series are shown in Figure (3.5). It is possible to observe that at hourly scale there are components with periods: $T_1 = 1/0.0001143 \simeq 8748$ hours $\simeq 1$ year, $T_2 = 1/0.04167 \simeq 24$ hours. At daily scale only a component is evident corresponding to a period of $T_3 = 1/0.002743 \simeq 365$ days, i.e. 1 year. The absolute slopes of hourly and daily average wind speed power spectra computed for some of the considered stations are reported in Table 3.3. As it is possible to see for the stations referred as Aberdeen, Chiari, Como, Lambrate and Vercana the slopes both at hourly and daily scale are in the range $\beta \in [0.51.5]$, thus meaning that performs as $1/f$

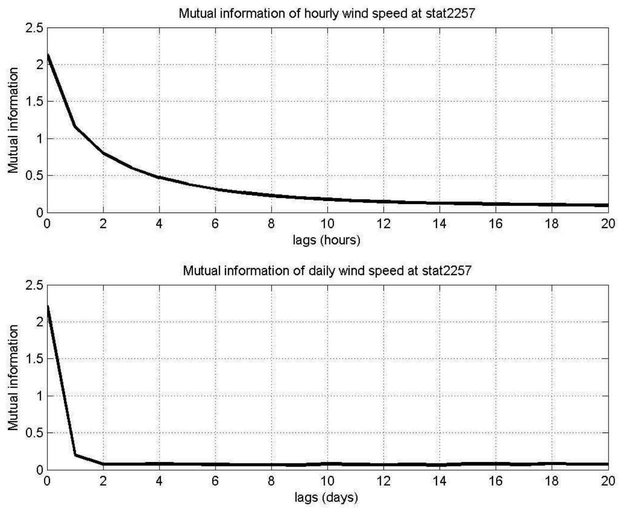

Fig. 3.4. Mutual information of hourly and daily average wind speed time series at the ID2257 station.

station	$\beta(hourly)$	$\beta(Daily)$
Aberdeen	1.50	0.80
ID2257	2.01	0.96
ID2300	2.03	0.92
ID6435	1.87	0.74
ID9004	1.84	0.78
Chiari	1.44	0.62
Como	1.26	0.67
Lambrate	1.34	0.71
Vercana	1.55	0.74

Table 3.1. Absolute slopes of hourly and daily average power spectra at various stations in USA and Italy

noise. Instead, for the stations referred to as ID2257, ID2300,ID6435 and ID9004, the time series exhibit absolute slopes almost close to

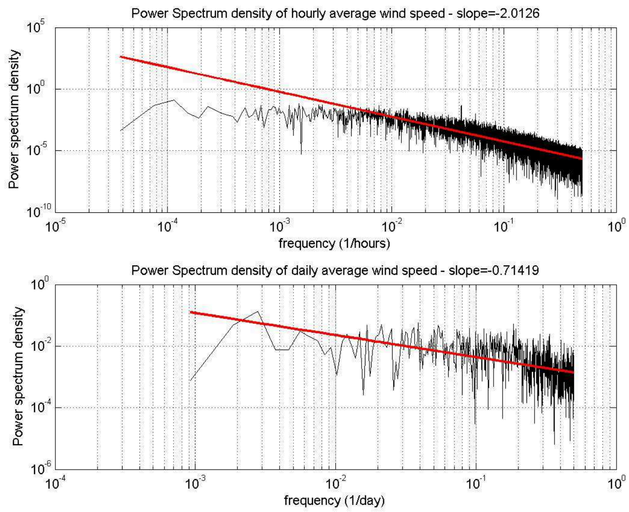

Fig. 3.5. Power spectrum densities of hourly and daily average solar radiation time series at the station ID2257.

2, thus behaving as random walks. The peculiarity of these latter stations is that wind is recorded at 100 m above sea level.

3.4 Hurst Exponent and Fractal dimension

The Hurst exponents and the fractal dimensions of hourly average wind speed computed for each year during 2004 to 2006 is shown in Figure (3.6). The Hurst exponent was computed by using the R/S algorithm while the fractal dimension was computed by using the boxcounting algorithm. It is possible to see that on average the Hurst exponent is 0.74 while the fractal dimension is 1.38. Thus the Hurst exponent is almost in the range 0.73 ± 0.09, observed for several natural systems. The Hurst exponent computed at nine

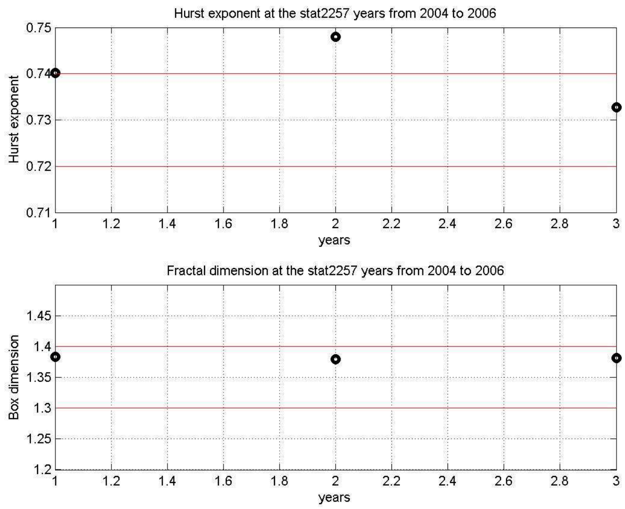

Fig. 3.6. Hurst exponent and Fractal dimension of hourly average wind speed at the station ID2257.

different recording stations by using three different algorithms [10], namely the R/S, the DFA and GPH, are given in Figure (3.7). As it possible to see there are clear differences among different algorithms. However all algorithms confirms that, independently from the considered recording stations and algorithm, wind speed time series are fractal and long range correlated, since the Hurst exponent are in the range $0.5 < H \leq 1$.

3.5 Multifractal Spectrum

Results of multifractal detrended fluctuation analysis performed on hourly average wind speed time series are shown in Figure (3.8). Roughly speaking this Figure shows that wind speed time series,

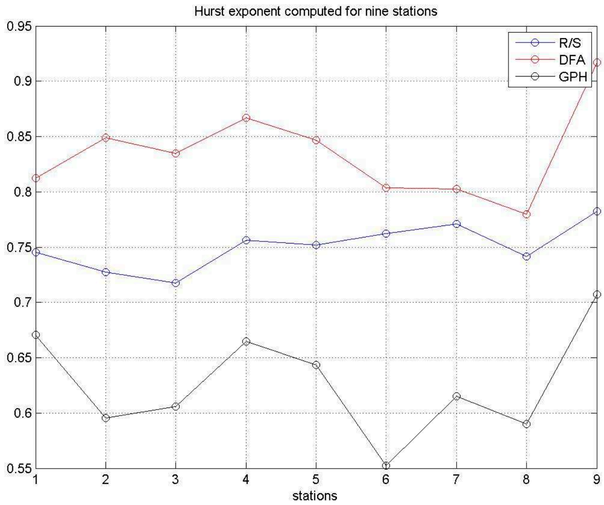

Fig. 3.7. Hurst exponent computed at nine recording stations by three different approaches. The nine recording stations are: $1 = Aberdeen$,$2 = ID2257$,$3 = ID2300$,$4 = ID6435$,$5 = ID9004$,$6 = ID9004$,$7 = Chiari$,$8 = Como$,$9 = Vercana$

similarly to solar radiation time series, are multifractal. A detailed interpretation of this Figure is similar to that given in section 2.6 for the multifractal spectrum of solar radiation time series.

The generalized Hurst exponent and the corresponding multi fractal spectrum at various wind speed recording stations in USA and in Italy are shown in Figure (3.9) and Figure (3.10), respectively.

Figure (3.9a) and (3.10.a) show that the generalized Hurst exponent $H(q)$ significantly varies versus q, thus meaning the clear multifractal nature of wind speed time series at all the considered stations, independently on the geographical area and altitude. In particular, bearing in mind that $H(2)$, i.e. the generalized Hurst exponent obtained for $q = 2$, represents the Hurst exponent given

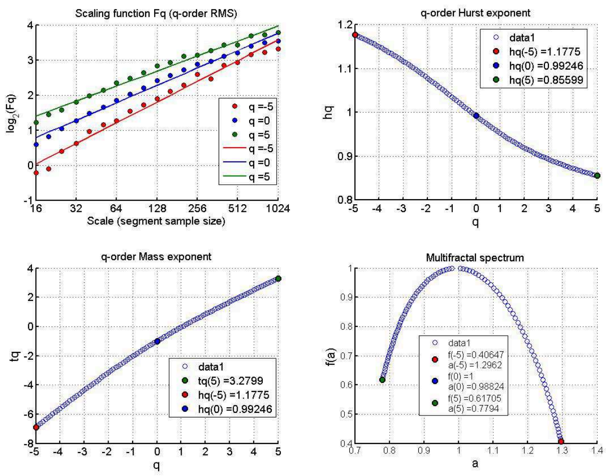

Fig. 3.8. Multifractal spectrum at station ID2257

by the traditional monofractal DFA (Detrended Fluctuation Analysis), it is possible to see that such particular values are in the range $H \in [0.65, 0.75]$ and $H \in [0.7, 0.75]$ for the USA and Italy stations, respectively. Such a difference can be explained looking at the altitude (from the ground, or from the sea) at which wind speed is sampled and at the different altitude above sea level of the recording stations. Indeed stations referred to as ID2257, ID2300, ID6435 and ID9400 samples wind speed at 100 m from the ground (or form the sea, in case of offshore plants), while the remaining stations samples wind speed at 10 m from the ground. Furthermore stations ID2257, ID2300 belongs to offshore plants while stations ID6435, ID9400 and Aberdeen are located at about 1700, 2100 and 1437 a.s.l., respectively.

Figures (3.9b) and (3.10.b) show the singularity spectra computed

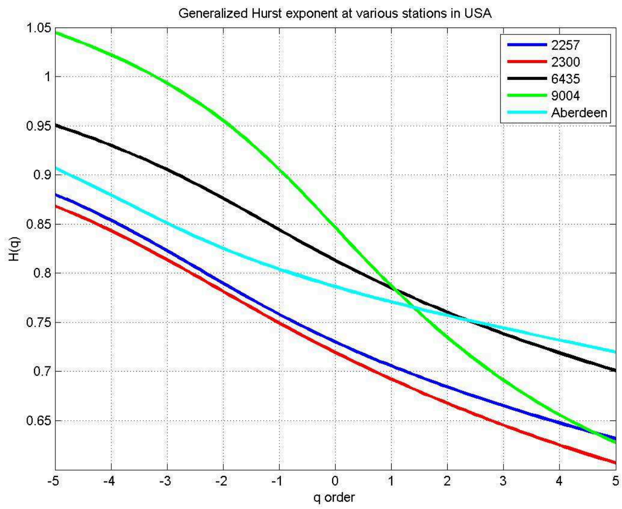

(a)

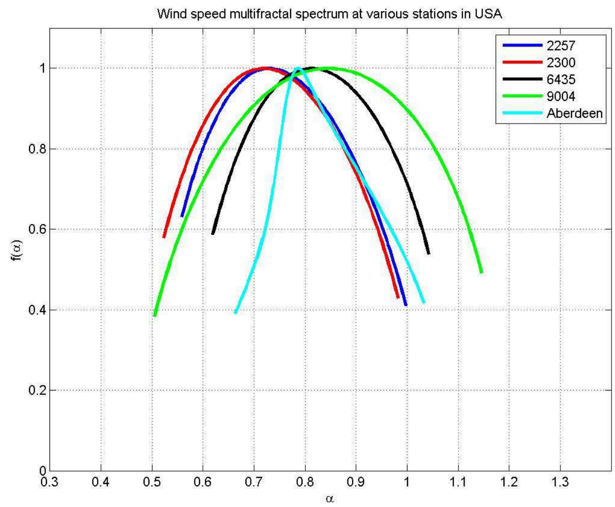

(b)

Fig. 3.9. Generalized Hurst exponent and multifractal spectrum at various recording wind speed recording stations in USA (a) Generalized Hurst (b) Multifractal Spectrum

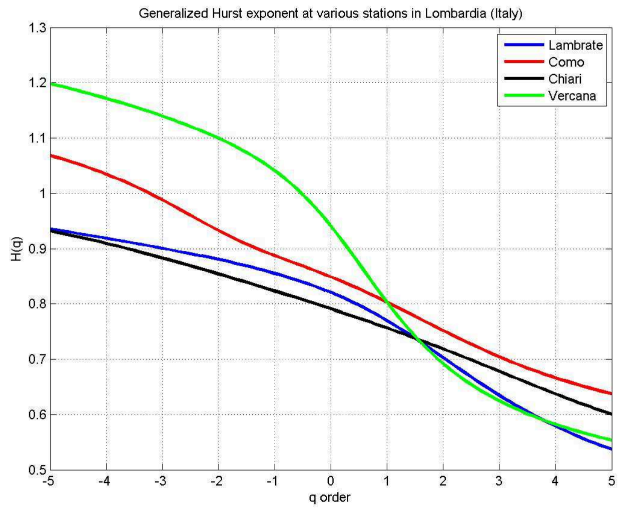

(a)

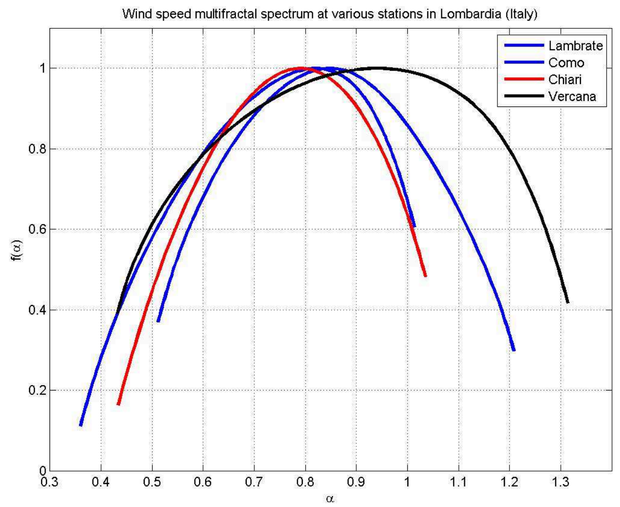

(b)

Fig. 3.10. Generalized Hurst exponent and multifractal spectrum at various recording wind speed recording stations in Lombardia (Italy) (a) Generalized Hurst (b) Multifractal Spectrum

for the recording stations in USA and in Italy, respectively. From these Figures it is evident that the features of the singularity spectra are significantly affected by the different operating conditions of wind speed recording stations. This aspect, which seems to me quite intriguing, is leaved for future developments of this research.

3.6 Estimation of the embedding dimension

In order to determine the embedding dimension m of wind speed time series, I have evaluated the fraction of false nearest neighbors versus m, as shown in Figure (3.11). The Figure shows that, simi-

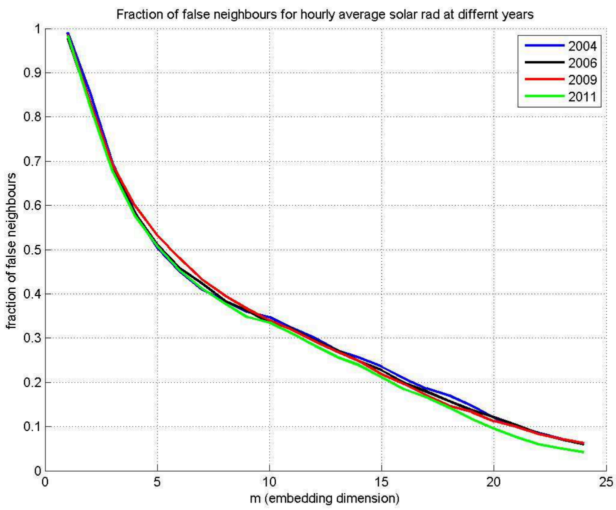

Fig. 3.11. Fraction of false nearest neighbors of solar radiation at Lambrate during 2012

larly to what observed for solar radiation time series, the fraction of false nearest neighbors decays slowly with the embedding dimension and a small fraction is computed also for $m = 24$. This results may be due to noise effecting the data.

3.7 Maximal Lyapunov exponent

I have estimated the maximal Lyapunov exponent of hourly average wind speed by using the approach described in [11]. Computation performed with the *Lyap_spec* program, which is part of the Tisean package gives a value of 0.121. It is interesting to observe that similar values was observed for all considered recording stations. Furthermore, not only the largest Lyapunov exponent are almost equal but the overall Lyapunov spectrum, as shown in Figure (3.12).

3.8 Conclusions

Analysis presented in this chapter, performed on both hourly and daily average wind speed time series allow to draw some conclusions about their nature. Stationary analysis, carried out by using different approaches, has not pointed out evidences that they are non stationary, at least in time interval of a few years, as analyzed in this work. Fractal analysis pointed out that these kind of time series are fractal and, in more detail, multi-fractal. Some kind of analysis carried out in order to see if there are evidences of low dimensional deterministic chaos in wind speed in time series, as claimed by ([8]), is not clear to me. Indeed, the search for an embedding dimension, performed in the range $[1, 24]$, pointed out that

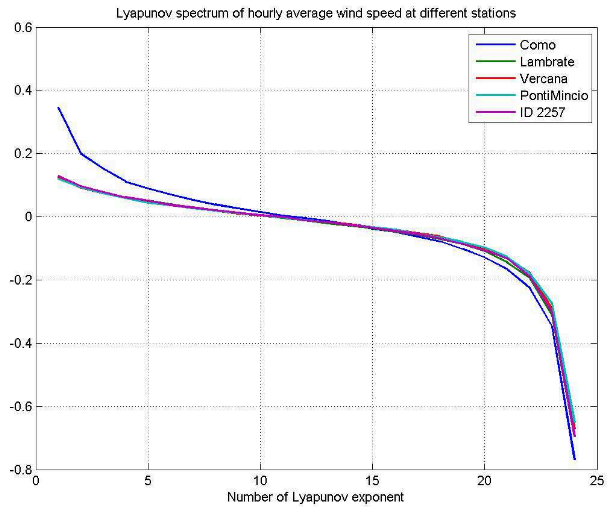

Fig. 3.12. Lyapunov spectrum of hourly average wind speed at 4 different recording stations

there is a fraction of false nearest neighbors also for high embedding values (e.g. $m = 24$), thus meaning that the supposed low dimensional chaotic attractor is not realistic. However, this results can also be explained as the effect of random noise which affect the dataset. On the other hand the computation of the maximal Lyapunov exponent and of the whole Lyapunov spectrum pointed out the presence of one or more positive exponents. However, the spectral analysis show that wind speed time series, belongs to the class of $1/f$ noise or in same case to random walks.

4

Time series models for wind speed and solar radiation

Research efforts in the area of wind speed and solar radiation time series forecasting started in the eighties and has becoming continuously increasing and nowadays some hundred thousand of scientific papers are available. However, since standard protocols are not considered to assess the features of the proposed models, it is very difficult, or even impossible, to inter-compare different techniques from literature results.
Referring to the subject of wind speed time series forecasting several review papers have been published such as [12],[13],[14],[15],[16], and [17]. Nevertheless, most of the paper agree to indicate that statistical models perform well when the forecasting horizon is only a few hours.
After the earliest attempt to predict wind speed time series by using Kalman models [18], a huge number of techniques have been considered such as ARMA (Auto Regressive Moving Average) models [19],[20],[21], ARMA-GARCH (Generalized Autoregressive Conditional Heteroskedasticity) [22], ARIMA and ANN (Artificial Neural Networks) [23],[24], Hybrid models ARMA and TDNN (Time

Delay Neural Networks) [25], ANN (Artificial Neural Networks) [26],[27],[28], Soft-Computing models [29], ANFIS (Adaptive Neural Fuzzy Systems) [30], Generalized mapping regressors [31], Marcov chains [32], Principal Component Phase Space Reconstruction [33], Multiple architecture system [34] and Spatial Correlation models [35]. However such a list of modeling techniques is not exhaustive.
Referring to the modeling of solar radiation time series, techniques similar to those referenced above for wind speed have been proposed. For instance, ARMA-GARCH models have been considered by [36], ARMA and TDNN by [37] and [38], Recurrent Neural Networks by [39], ANFIS and ANN by [40] and [41], Statistical time series models by [42], Decomposition models by [43], Fuzzy with Genetic Algorithms models by [44], Empirical mode decomposition by [45], Bayesian statistical models by [46], Machine learning by [47], Particle swarm optimization and evolutionary algorithm, using recurrent neural networks by [48]. Also in this case this list is far to be exhaustive.
In my PhD work, after trials with several of the approaches proposed in literature, I have decided to focus on the use of the NAR (Non-linear Auto Regressive) and EPS (Embedding Phase Space) model structures, identified by using ANFIS (Adaptive Neuro-Fuzzy Inference Systems) and ANN (Artificial Neural Networks) approaches, as described in the following section.

4.1 NAR and EPS time series models

A time series can be considered as a sequence of measurements $y(t)$ of an observable y performed at equal time intervals. The Takens theorem implies that for a wide class of deterministic systems, there exists a diffeomorphism (i.e. a one-to-one differential mapping) between a finite window of the time series $(y(t), y(t-1), ..., y(t-d+1)$ and the state of the dynamic system underlying the series. This implies that in theory there exist a MISO (Multi-Input Single-Output) mapping $f : R^n \rightarrow R$ such that

$$y(t+1) = f(y(t), y(t-1), ..., y(t-d+1)) \tag{4.1}$$

where d (dimension) is the number of considered past values. This formulation returns a state space description where, in the d dimensional state space, the time series evolution is a trajectory and each point represents a temporal pattern of length d. Prediction models of the kind (4.1) are usually referred as NAR (Nonlinear Auto-Regressive) models. These kind of models generalize into the so-called NARX (acronym of Nonlinear Auto-Regressive with eXogenous, i.e. external, inputs) model represented by expression (4.2)

$$y(t+1) = f(y(t), ..., y(t-d+1), u(t), ..., u(t-q+1)) \tag{4.2}$$

in presence of a vector $u(t)$ of explaining variables, i.e. variables that are in some way correlated with $y(t)$. NAR and NARX have a linear counterpart into AR and ARX which however are not usually appropriate to describe natural phenomena. Mapping of the kind (4.1) or (4.2) can be used in two ways: one-step prediction and iterated prediction. In the first case, the d previous values of the series are assumed to be available and the problem is equivalent to a function estimation. In the case of iterated prediction, the predicted output is feedback as an input to the following prediction. Hence, the inputs consist of predicted values as opposed to actual observations of the original time series. A prediction iterated for k times returns a k-step-ahead forecasting. The task of forecasting a time series over a long horizon is commonly tackled by iterating one-step-ahead predictors. Despite the popularity that this approach gained in the prediction community, its design is still affected by a number of important unresolved issues, the most important being the accumulation of prediction errors. In my experience, iterated forecasting does not work after a very few steps. Another problem dealing with NAR (and NARX) models is that the regressors $(y(t), y(t-1), ..., y(t-d+1)$ of the output variable are the most recent past variables, which very often are correlated each other, i.e. are not really independent variables. To avoid using consecutive regressors of $y(t)$ it is possible to modify the regressor vector as $(y(t), y(t-\tau), ..., y(t-(d-1)\tau))$, i.e. the regressors are time-spaced by τ steps and thus expression ((4.1)) could be modified as in expression (4.3).

$$y(t+1) = f(y(t), y(t-\tau), ..., y(t-(d-1)\tau)) \tag{4.3}$$

The τ parameter is usually chosen with the criterion of the first minimum of the mutual information, which assures that two consecutive regressors of the f function are few correlated and thus almost independent. These ideas are inspired by the so-called Embedded Phase-Space (EPS) representation of dynamical systems which are largely considered in non-linear modeling of chaotic time series. Of course expression (4.3) reduces to the traditional NAR form (4.1) when $\tau = 1$. In the framework of EPS models the parameter τ is referred to as *delay* while d is referred to as the *embedded* *dimension* and can be chosen by using various criteria such as, for instance, evaluating the fraction of false neighbors.

4.2 Multi-step ahead prediction models

The MISO map (4.3) can be appropriately extended for multi-step prediction according with expression (4.4).

$$\begin{aligned} y(t+h) =& f(y(t), y(t-\tau), ..., y(t-(d-1)\tau) \\ h =& 1, 2, ...24 \end{aligned} \tag{4.4}$$

In other terms, in order to perform multi-step prediction avoiding to use iteratively expression (4.2), which as mentioned fails after a few step due to accumulation error, it is proposed to directly mapping the input vector $[y(t), y(t-\tau), ..., y(t-(d-1)\tau]$ to the output scalar $y(t+h)$ by using two different neural network based approach, namely the Neuro-Fuzzy (NF) and the Feedforward Neural Network (NN) approaches. The mapping will be performed for prediction horizon h in the range $1 \leq h \leq 24$ hours. The two mapping approaches are shortly outlines in the next sections.

4.3 Mapping approximation

Neural Networks based approaches are among the most popular and efficient tools to approximating a map f of the kind considered in this work. In particular, I have considered two kinds of approaches namely the Neuro-Fuzzy and the Feedforward Neural Networks approaches, respectively. One of the main advantages of these approaches is that, roughly speaking, they allow to approximate nonlinear maps by various kinds of basis function, such as, sigmoidal, gaussian, wavelet and so on. In particular the gaussian basis functions seems particularly appropriate for solar radiation time series modeling, due to the gaussian shape of daily solar time series.

4.3.1 The Neuro Fuzzy approach

One of the most interesting aspects of the NeuroFuzzy approach is that once the neural network has been trained by using automatic learning algorithms, the obtained model can be interpreted in terms of a base of *if ... then* rules. The resulting models can be represented both in linguistic form, or as multidimensional surfaces, whose coordinates are the arguments of the f function. In particular, if the rules are expressed in the so-called Takagi-Sugeno form [49], i.e with the consequent part expressed as a linear combination of the input mapping, often the model surfaces are iperplanes and thus the rule base can be approximated by simple mathematical expressions. Identification of the model rule base can be obtained in several ways. In particular I have considered the *genfis3.m* function which is part of the Maltab fuzzy toolbox. This function generates a FIS (Fuzzy Inference System) by using the fuzzy c-means (FCM) clustering algorithm. Gaussian type functions were considered to represent the membership functions. For each of the argument that appears in the f function, three membership functions were considered to describe what is usually referred the *universe of discourse*. In this work, the combination of the Embedded Phase Space model structure and the Neuro-Fuzzy neural networks for approximating the f map, will be referred, to as the EPSNF approach.

4.3.2 The FeedForward Neural Network Approach

Feedforward networks consist of a number of simple artificial neurons, organized in layers. The first layer has a connection from the network input. Each subsequent layer has a connection from the previous layer. The final layer produces the network's output. Such a kind of networks can be used for many kinds of input to output mapping. A feedforward network with at least one hidden layer and enough neurons can fit any finite input-output mapping problems. Several kind of different training algorithm can be used to training the network, such as for instance the popular Levenberg-Marquardt optimization algorithm which was taken into account in this work. Since in this case feedforward neural networks are considered for approximating the f map, the approach will be referred to as EP-SNN.

4.4 Conclusions

A huge number of techniques have been proposed in literature to model solar radiation and wind speed time series and thus it is almost impossible to be exhaustive dealing with this subject. For this reason, the description was limited to the NARX and to the Embedded Phase-Space approaches, which were considered the most appropriate for the purposes of this work.

5

Modeling hourly average solar radiation time series

In this section results obtained by applying the modeling approaches described in Chap. 4 to a data set of hourly average time series recorded from 2011 to 2013 are reported. For all modeling trials, data recorded during 2011 and 2012 was considered to identify the model parameters while remaining data was reserved to test the model. Model performances have been evaluated by considering the traditional *mae* and *rmse* error indices.

5.1 Performances of the NARX Neuro-Fuzzy modeling approach

One of the interesting aspects of applying the Neuro-Fuzzy technique to the considered problem is that it is often possible to obtain quite simple approximated models which relate the solar radiation at some time $(t + h)$ and others meteorological variables recorded at the same station until time t. The description starts showing results obtained by the simple model of the form (5.1), where the prediction horizon has been set to $h = 0$, which means a pure static input-output model, with the aim of evaluating to what extent the hourly average solar radiation at time t can be explained as a function of the hourly average values of temperature, pressure and relative humidity recorded at the same hour.

$$sr(t) = f(ws(t), te(t), pr(t), hum(t)) \tag{5.1}$$

The Neuro-Fuzzy model obtained, graphically represented in terms of surfaces in three dimensional spaces, consists of planes, as shown in Figure (5.1) and thus a simple mathematical representation of the model is possible, as expressed by equation (5.2).

$$\begin{aligned} sr(t) =& 13.8 \cdot ws(t) + 7.3 \cdot te(t) + 1.74 \cdot pr(t) \\ & - 2.5 \cdot hum(t) - 1615 \end{aligned} \tag{5.2}$$

The time behavior of such a model, represented in Figure (5.2), shows that it perform poorly, i.e. it is only partially able to capture the true relation among solar radiation and the other considered explaining variables. On the other hand the hourly averages of solar radiation are weekly correlated with the explaining variables considered in equation (5.2). For short time horizons, such a behavior can be significantly improved, by adding and autoregressive term, i.e. considering, in the simplest case, a model of the form (5.3).

$$\begin{aligned} sr(t+h) =& f(sr(t), ws(t), te(t), pr(t), hum(t)), \\ & h = 1, 2, ... \end{aligned} \tag{5.3}$$

as shown in Figure (5.3) for $h = 1$. It is evident that adding at least one regression of the output into the list of the f arguments improves the capability of the model to predict future values (com-

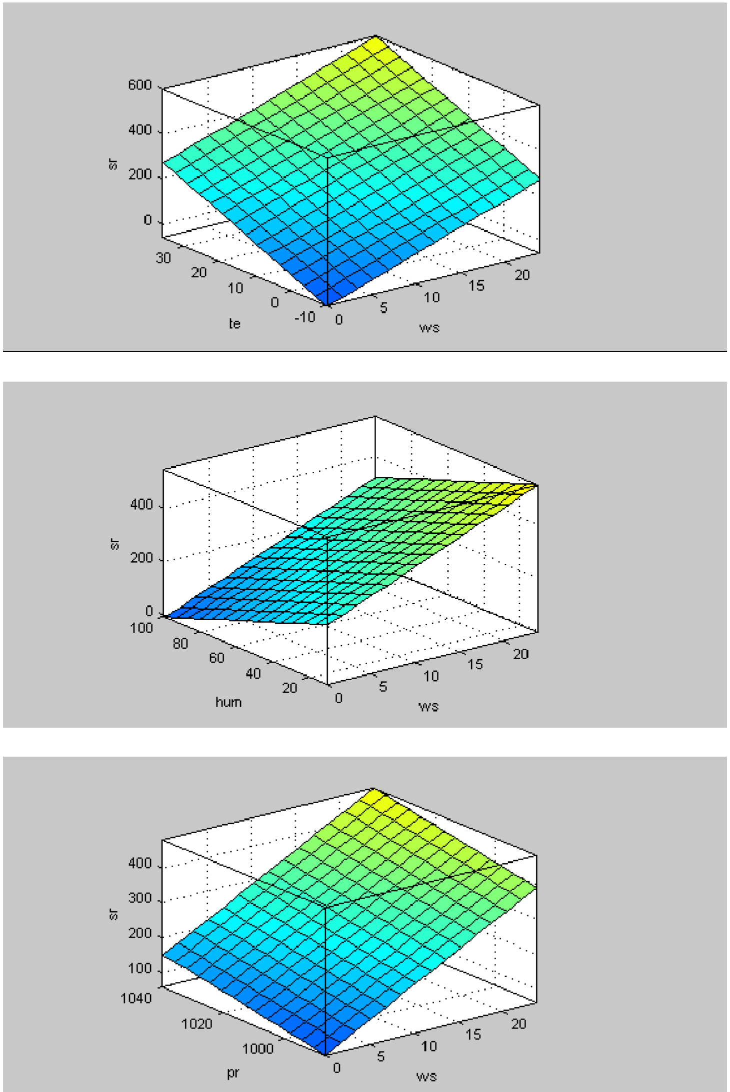

Fig. 5.1. Surfaces of the NF model (a) sr-ws-te (b) sr-hum-ws (c) sr-pr-ws.

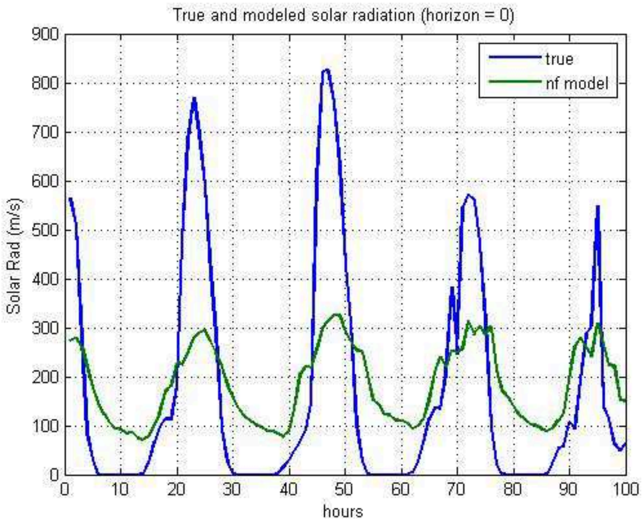

Fig. 5.2. True and modeled time series by a NARX NF model expressed by equation 5.1 (h=0).

pare the behavior shown in Figure (5.2) with that shown in Figure(5.3). In order to objectively evaluate the performance of NF models of the form (5.3) for the whole range $1 \leq h \leq 24$ of prediction horizon, two error indices were computed: the *mae* (mean absolute error) and the *rmse* (root square mean error), defined as expressed in (5.4) and (5.5), respectively.

$$mae = \frac{1}{n}\sum_{i=1}^{n}|y(i) - \hat{y}(i)| \tag{5.4}$$

$$rmse = \sqrt{\frac{1}{n}\sum_{i=1}^{n}(y(i) - \hat{y}(i))^2} \tag{5.5}$$

where n is the number of samples considered to compute the error indices and the symbol $\hat{y}$ indicates the estimated sample. Fur-

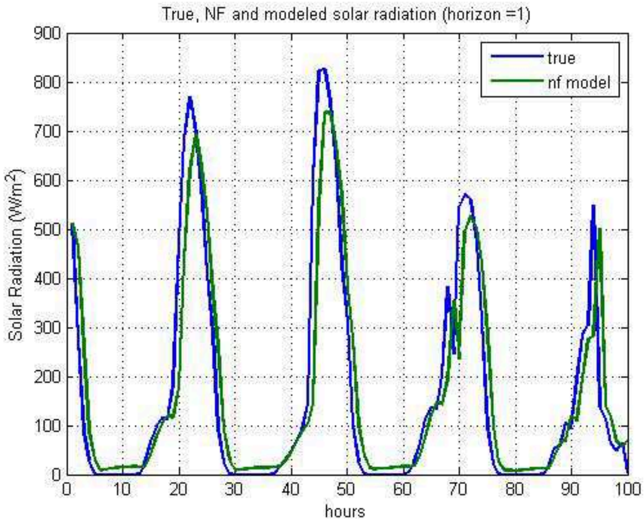

Fig. 5.3. True and modeled time series by a NARX NF model expressed by equation (5.3) (h=1).

thermore the NF model performance was compared with that of a persistent model, i.e. a model characterized by the simple equation (5.6), which is often considered as a reference model.

$$\hat{y}(t+h) = y(t) \tag{5.6}$$

From results shown in Figure (5.4) it is possible to see that:

1. for $1 \leq h \leq 4$, the model (5.3) performs exactly as the persistent model and thus there is not convenience on using it.
2. The *mae* and *rmse*, increases faster for the persistent model with respect to the NF model. Furthermore, while for the NF model the error reaches a maximum value for $h = 5$, for the persistent model the error curve is almost symmetric and reaches a maximum for $h = 12$, i.e. half of a day. For $h > 12$ the persistent

model error start decreasing and for $h = 24$ again approaches values comparable to that of the NF model.

3. for $21 \leq h \leq 24$ again the NF model performs as the persistent.
4. Although the NF model outperform the persistent model for prediction horizon in the range $5 \leq h \leq 20$, this does not imply that its performance are acceptable for forecasting purpose, even at short time horizon. For instance, its time behavior for $h = 3$ is shown in Figure (5.5), which reveals that the model is not reliable to predict the peak values of the true time series.

5.2 Performances of the NARNF approach

In this section models of the form 4.1, for different values of the delay d in the range $[3, 24]$ are considered. The *mae* and *rmse* errors obtained for this kind of models are shown in Figure (5.6). It is possible to see that NARNF models featured by $\tau = 1$ do not exhibits a uniform error versus h in the overall explored range, unless the dimension d is set to $d = 24$. Instead, the NARNF model with an embedding dimension $d = 24$ perform quite well, not only for short prediction horizons but in the whole range $[1, 24]$ since the *mae* and rmse curves are flat. In terms of performance indices, it is possible to say that $mae \leq 50W/m^2$ and $rmse \leq 90W/m^2$ in the whole explored range.

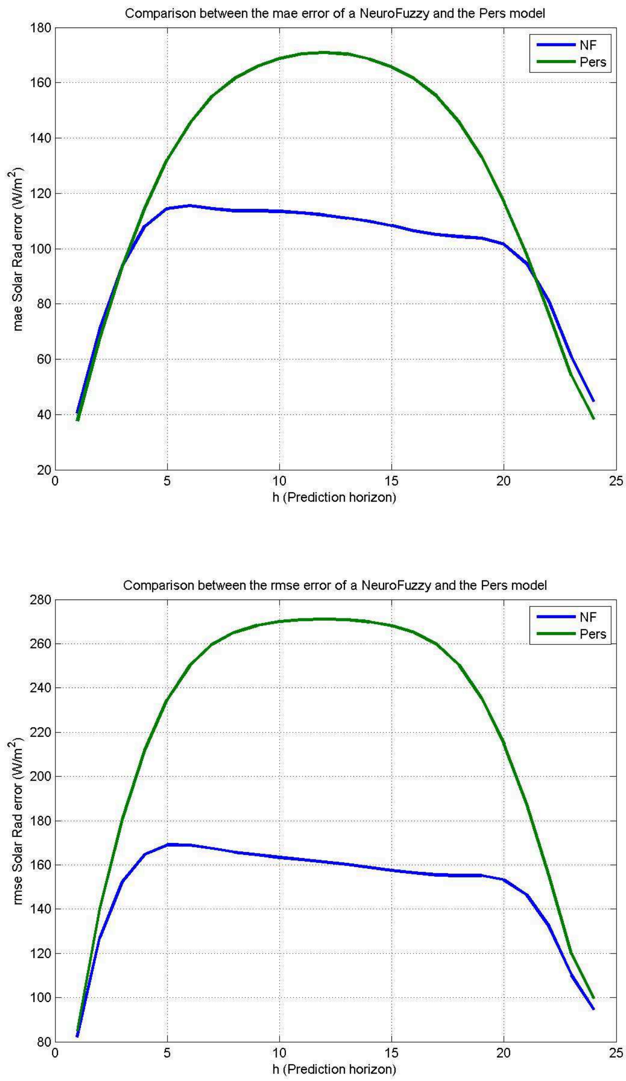

Fig. 5.4. Performance of the NARX NF model (a) MAE (b) rmse.

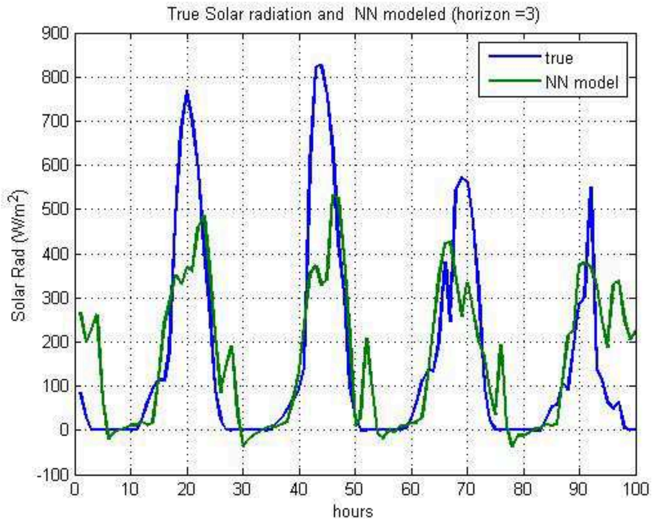

Fig. 5.5. True and modeled time series by a NARX NF model (h=3).

5.3 Performances of the EPS Neuro-Fuzzy modeling approach

In this section I show results obtained considering embedding phase-space models of the form (5.7),

$$\begin{aligned} sr(t+h) = & f(sr(t), sr(t-\tau), ..., sr(t-(d-1)\tau) \\ & h = 1, 2, ...24 \end{aligned} \tag{5.7}$$

where, again, the unknown mapping function f is identified by the neuro fuzzy approach. In the rest of the work this kind of models will be referred to as EPSNF (acronym of Embedded Phase-Space Neuro-Fuzzy). Since the most appropriate value for the embedding dimensions is unknown, a series of trials were performed assuming that d is an integer value in the range $3 \leq d \leq 24$. As concerning the

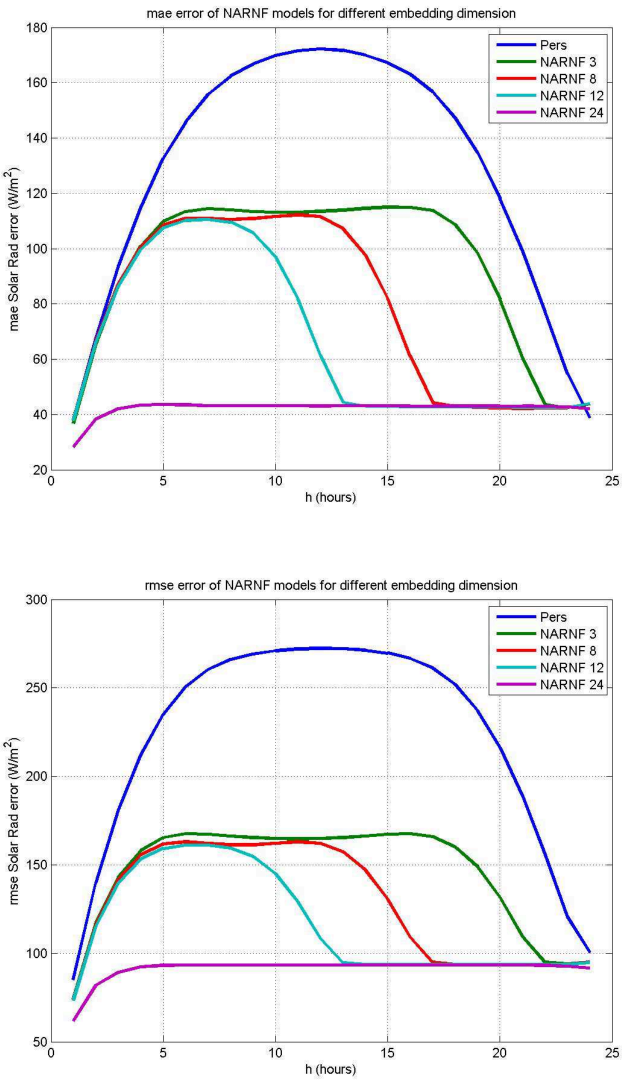

Fig. 5.6. Performances of the NARNF model for $d \in [3, 8, 12, 24]$ (a) mae (b)rmse.

delay τ, two series of trials were performed. The first trial assumes $\tau = 1$, since this is the case when the EPS model reduces to the popular NAR model. The second series of trial refers to different values $\tau > 1$.

5.4 Performances of the EPSNF approach

In this section prediction models of the form (4.3) identified by using the NF mapping approach are considered by setting the time delay parameter $\tau = 2$ and for various values of d in the range $[3, 24]$. The performance in terms of *mae* and *rmse* are shown in Figure (5.7). It is possible to see that NAR NF models do not exhibits a uniform error versus h in the overall explored range, unless the dimension d is set to $d = 12$. Thus it was experimentally found that an EPS model with 12 regressors perform as a NAR model with 24 regressors, provided that the 12 regressors are chosen assuming $\tau = 2$. This results can be explained bearing in mind that hourly average solar radiation time series exhibits a strongly periodic behavior with a 24 hours period and that by using 12 regressors delayed by $\tau = 2$ it is possible to cover the whole 24 hours time interval. Furthermore, it is to stress here that the search for an embedding dimension for hourly average solar radiation time series, by using the false-neighbors algorithm suggested an embedding dimension ≥ 24. This result allows to conjecture that to implement a prediction model with flat *mae* and *rmse* errors in the whole range $[1, 24]$, it is required, that $d \cdot \tau \geq 24$. Such a conjecture was experimentally verified to be true as shown in Figure (5.8). It is possible to observe that the error curves, obtained assuming $d \cdot \tau = 8 \cdot 3 = 24$

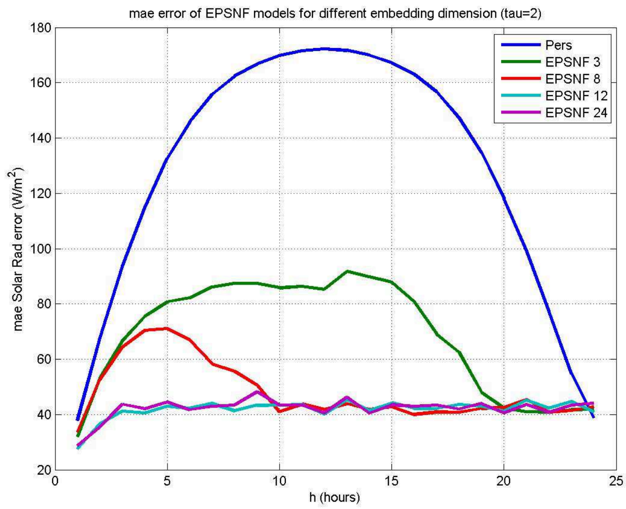

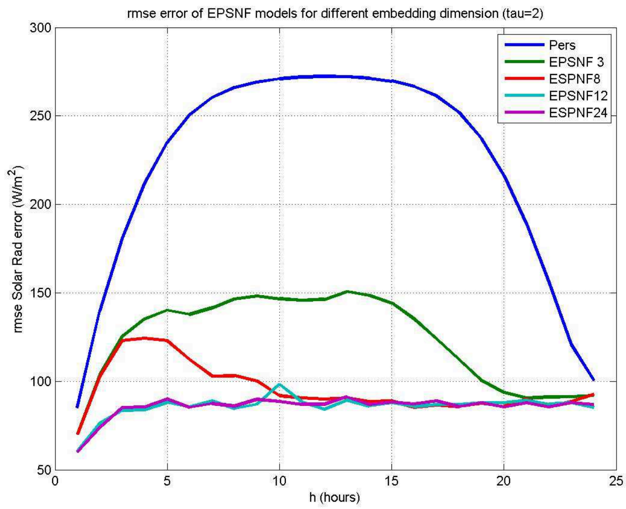

Fig. 5.7. Performances of the EPSNF $\tau = 2$ and $d \in [3, 8, 12, 24]$ (a) mae (b)rmse.

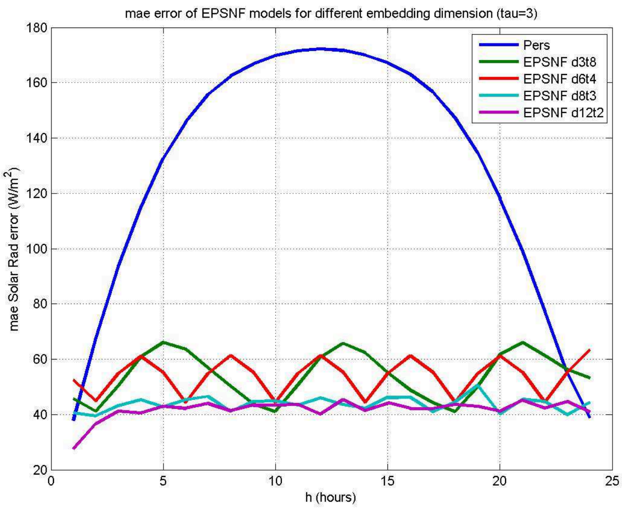

Fig. 5.8. mae versus the horizon for an EPSNF model ($d \cdot \tau = 24$).

works as well as the model featured by $d \cdot \tau = 12 \cdot 2 = 24$. However the figure shows that there is a minimum value for the number of regressors. Indeed, for instance choosing $d = 8$ and $\tau = 3$ or $d = 6$ and $\tau = 4$ do not give flat error over the explored range. Thus the rules should be modified as follow: to obtain an almost flat error it is necessary that both these to relations hold: $d \cdot \tau \geq 24$ and $\tau \leq 3$. To further stress the convenience of using the NF approach in conjunction with the EPS model structure it is reported in equation (5.8), the mathematical representation of an EPSNF model having $(d = 8, \tau = 3)$ and $h = 5$.

$$
\begin{aligned}
sr(t+5) =& 0.0510 sr(t) + 0.7866 sr(t-3) + 0.0796 sr(t-6) + \\
& - 0.0383 sr(t-9) - 0.0144 sr(t-12) - 0.0041 sr(t-15) + \\
& - 0.0342 sr(t-18) - 0.0008 sr(t-21) + 16.1475
\end{aligned}
\tag{5.8}
$$

which is quite simple to implement.

5.5 Performances of the NARNN approach

In this section performance of EPSNN, here considered as the acronym of Embedded Phase-Space Neural Network models will be shortly reported. For the lack of brevity, it is possible to say that considerations already expressed in the previous section for models EPSNF can also be applied to models EPSNN. For instance, the performance of the EPSNN model (5.7), in terms of *mae* and *rmse* errors are synthesized in Figure (5.9) for various embedding dimension d and also in comparison with the persistent model. The Figure shows that the EPSNN models significantly outperform the persistent model for any value for the embedding in the range considered ($3 \leq d \leq 24$). It is worth nothing that the performance for $d = 12$ and $d = 24$ are almost identical, thus demonstrating experimentally that, as already shown for models EPSNF $d = 12$ is probably the most appropriate size of the embedding for the considered problem, when using the NAR model structure. Another interesting aspect is that performance of this kind of models are almost independent on the prediction horizon in the range $1 \leq h \leq 24$.

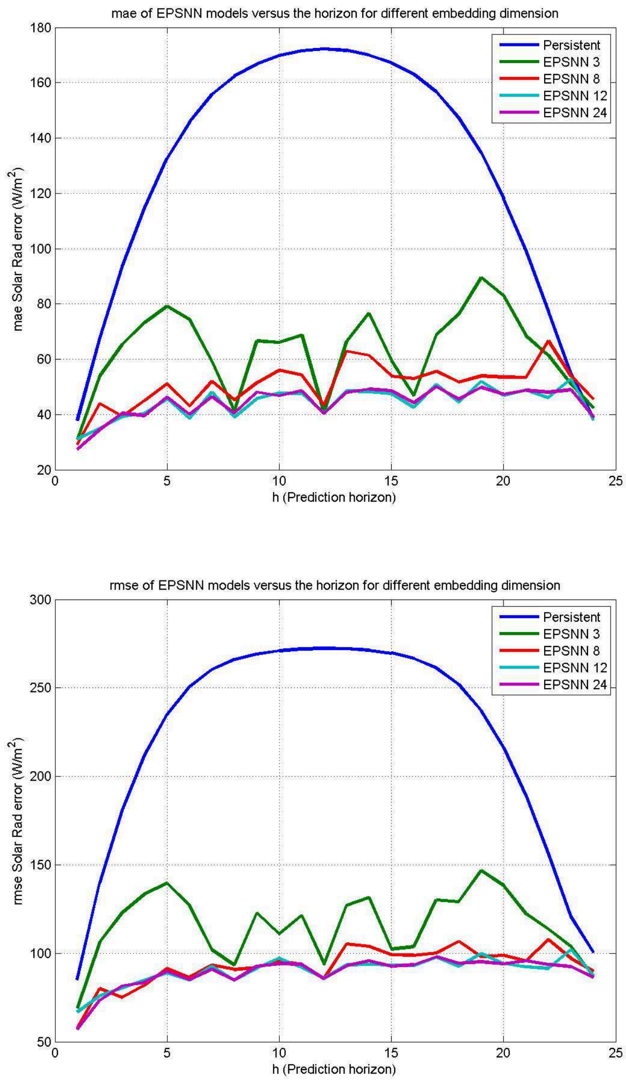

Fig. 5.9. Performances of the EPSNN models for $\tau = 1$ and $d \in [3, 8, 12, 24]$(a) mae (b)rmse.

5.6 A direct comparison between the EPSNF and EPSNN approaches

A direct comparison between EPSNF and EPSNN models, working on the same data set, limited to embedding dimension of $d = 12$ and $d = 24$, is reported in Figure (5.10). The Figure shows that the EPSNN model with $d = 12$ is slightly more accurate than corresponding EPSNF model and therefore may be preferred, in this respect. However this small advantage may not be decisive since the EPSNF models allow a simple external representation with respect to EPSNN model. Further insights concerning the goodness of EPSNN models can be obtained from the analysis of the residual, i.e. the difference between the actual and the predicted time series. To this purpose, as an example, the autocorrelation of the true and residual time series corresponding the prediction with a time horizon of $h = 5$ is shown in Figure (5.11). It is possible to see that both the autocorrelation and the mutual information of the residual decay faster than that of the true time series and periodic behavior is strongly attenuated in the residual time series. The histogram of residual generated by the considered EPSNN model is shown in Figure (5.12). The Figure shows that the residue of solar radiation generated by the model considered is symmetrically distributed around zero. In more detail, the central bin is centered at the value -24.04 and almost 80% of residual samples are in the central bin, while the remaining 20% is distributed around two bins: one with the center around the -136.11 value and the other centered at 88.02 -value.

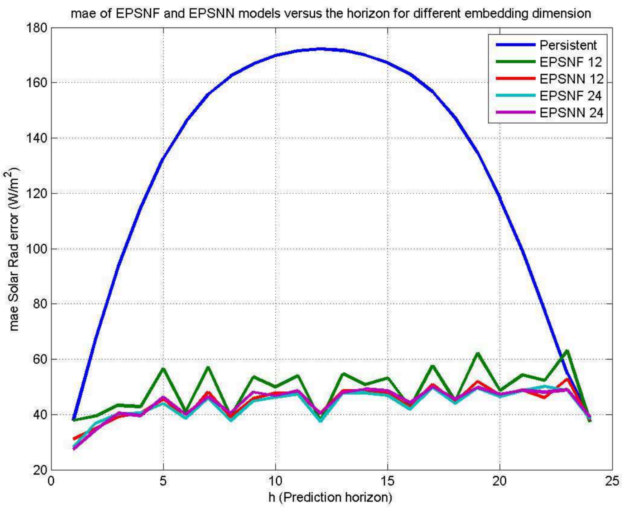

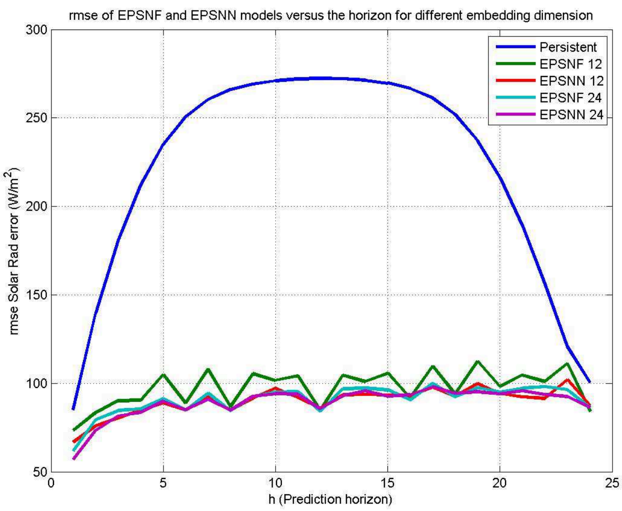

Fig. 5.10. Performances of EPSNF and EPSNN models for different embedding dimension (a) mae (b)rmse.

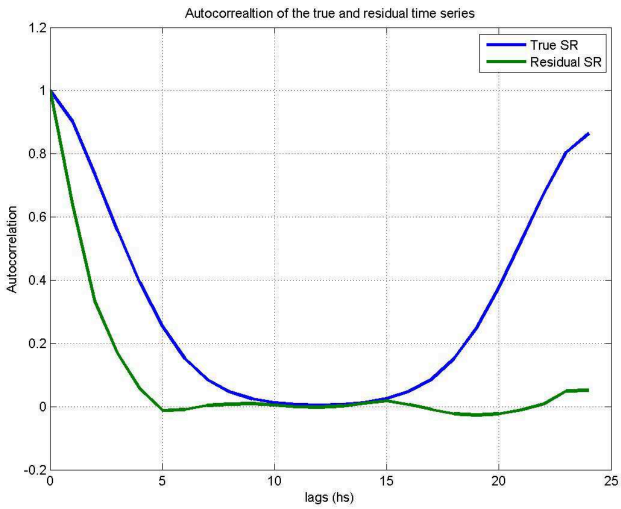

Fig. 5.11. Autocorrealtion and mutual information of the true and residual time series (h=5).

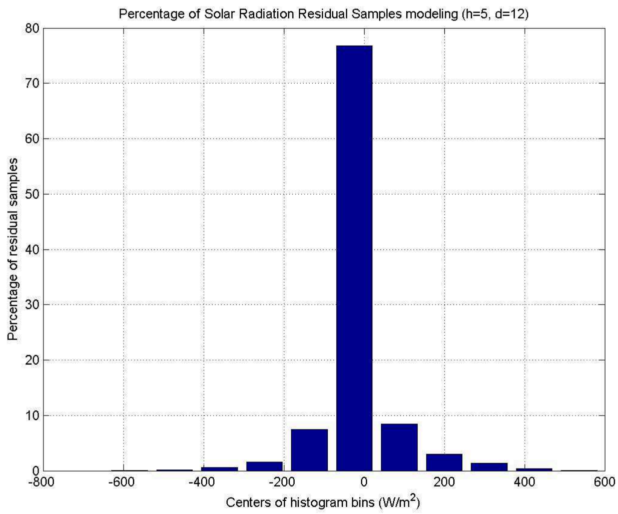

Fig. 5.12. Histogram of the residual generated by the EPSNN model ($h = 5, d = 12$)).

5.7 Conclusions

Results discussed in this chapter can be summarized as follows. Accuracy estimation of the prediction models, assessed in terms of mae and $rmse$ gives $mae \leq 50 Watt/m^2$ and $rmse \leq 80 Watt/m^2$, for the whole explored prediction horizon $h \in [1, 24]$. For very short prediction horizon, ($h \leq 3$), the performances are better since it has been found $mae \leq 40 Watt/m^2$ and $rmse \leq 60 Watt/m^2$. The studied models significantly outperform the persistent model in the whole explored prediction horizon $h \in [1, 24]$. The residue of solar radiation generated by the studied models is symmetrically distributed around zero and almost 80% of residual samples are in the central bin. The NF and NN approaches considered to identify the non-linear map underlying NARX and/or EPS models are comparable in terms of accuracy. However, NF prediction models could be preferred since allow a relative simple external representation.

6

Modeling hourly average wind speed time series

In this section results obtained by applying the modeling approaches described in Chap. 4 to the data set of hourly average time series recorded at Como (Italy) from 2011 to 2013, are discussed as a case of study. For all modeling trials, data recorded during 2011 and 2012 was considered to identify the model parameters while data recorded on 2013 was reserved to test the model. Model performances have been evaluated by considering the traditional *mae* and *rmse* error indices expressed by (5.4) and (5.5), respectively.

6.1 Performances of the NARNF approach

Following the same scheme adopted in the previous chapter devoted to solar radiation, I start the description of results obtained for wind speed time series from the simplest kind of NARX models, with the aim of evaluating to what extent solar radiation, temperature, air pressure and relative humidity may contribute to explain the wind speed dynamic at the considered recording site. Thus I have test the model described by (6.1)

$$ws(t+h) = f(sr(t), te(t), pr(t), hum(t)), h = 1, 2, ... \tag{6.1}$$

which relate the wind speed, $ws(t+h)$, at the time $t+h$, with solar radiation, $sr(t)$, air temperature, $te(t)$, air pressure, $pr(t)$ and relative humidity $hum(t)$ at time t. For each input variable three Gaussian membership functions were considered, generically indicated as *low, medium* end *high*, whose best parameters were obtained by the fuzzy c-means algorithm. The distribution of these membership functions in the so-called *universe of discourse* is shown in Figure (6.1), for each model input considered. The obtained model rule base is represented by three rules whose consequent part assumes, for $h = 1$, the form (6.2)

$$\begin{aligned} y(t+1) =& 0.0023sr(t) + 0.0061te(t) - 0.0761pr(t) \\ & - 0.0575hum(t) + 83.6348 \end{aligned} \tag{6.2}$$

Thus the model surfaces for $h = 1$ are the iper-planes shown also in Figure (6.2). The model surfaces obtained for $h = 4$ are shown in Figure (6.3). They are quite similar to those shown in Figure (6.2), thus meaning that for short prediction horizons the model parameters follows similar rules. The comparison between the true and the corresponding predicted time series, obtained by using the model (6.1), for $h = 1$, is shown in Figure (6.4).

It is possible to see that, although the true time series is more irregular than the computed one, the described model is able to explain the essential features of the input-output dynamics. It is to stress here that the output variable is not included as argument of the f model function and thus it not possible to attribute the

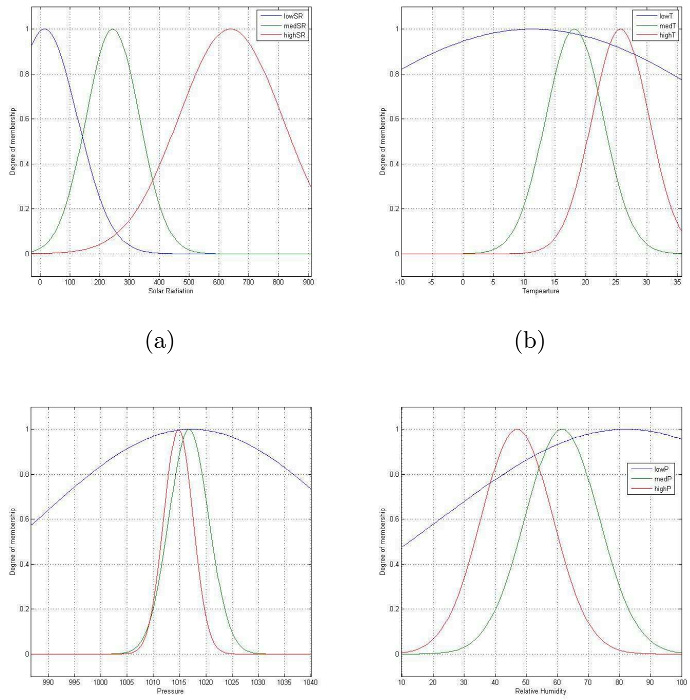

(a) (b) (c) (d)

Fig. 6.1. Gaussian type membership function computed by the fuzzy c-means algorithm in the framework of the genfis3 algorithm (a) Solar Radiation , (b) Temperature, (c) Pressure, (d) Relative Humidity.

model behavior to persistence of the output variable.
Simple prediction models as that expressed by (6.2) confirms what we know from analysis of daily patterns: the solar radiation and the air temperature are positive correlated with wind speed while the pressure and the relative humidity are negative correlated.
Since it is not reasonable the use of Neuro-Fuzzy models with a large

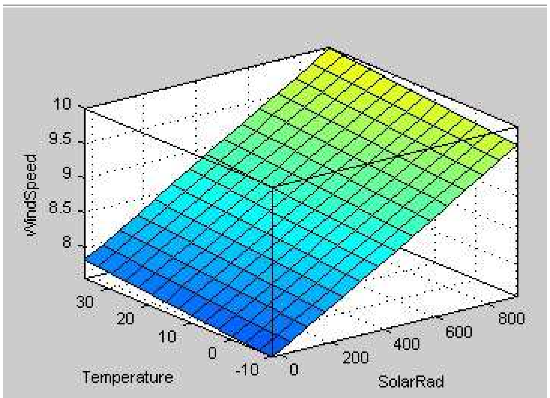

(a)

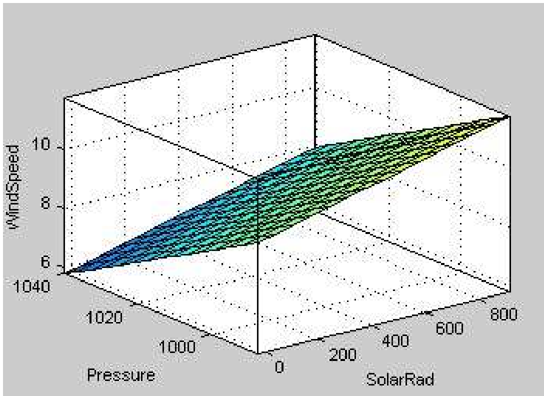

(b)

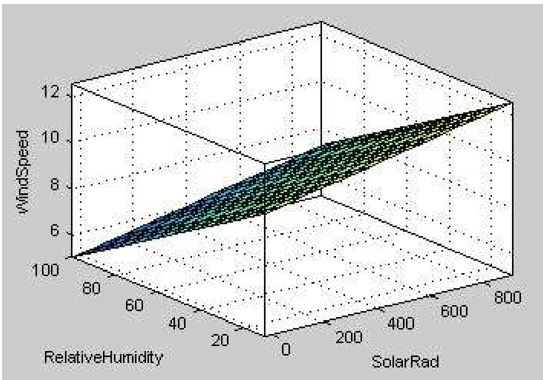

(c)

Fig. 6.2. Approximated linear relation between ws(t+1) and (a) sr(t), te(t) (b) sr(t),pr(t) (c) sr(t), hum(t).

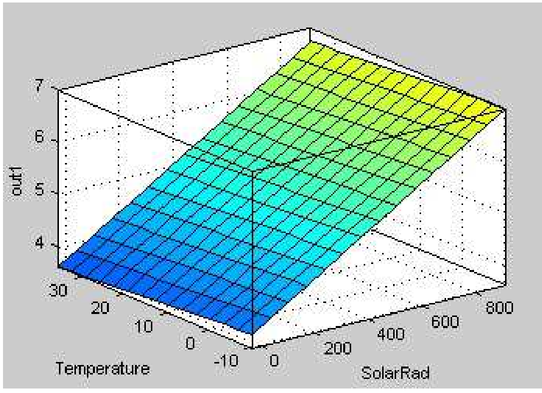

(a)

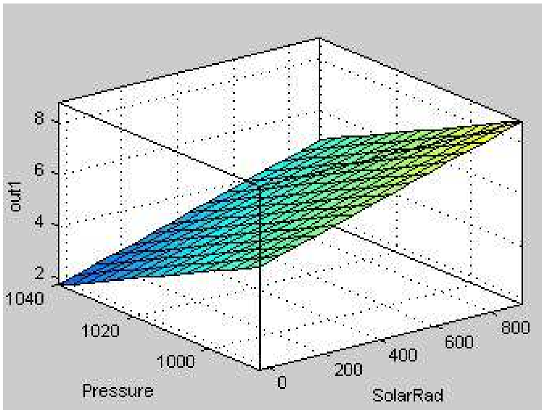

(b)

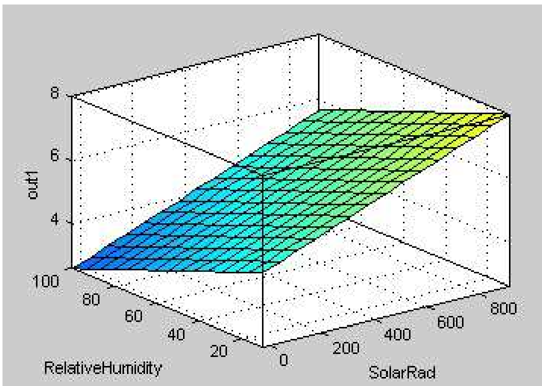

(c)

Fig. 6.3. Approximated linear relation between ws(t+4) and (a) sr(t), te(t) (b) sr(t),pr(t) (c) sr(t), hum(t).

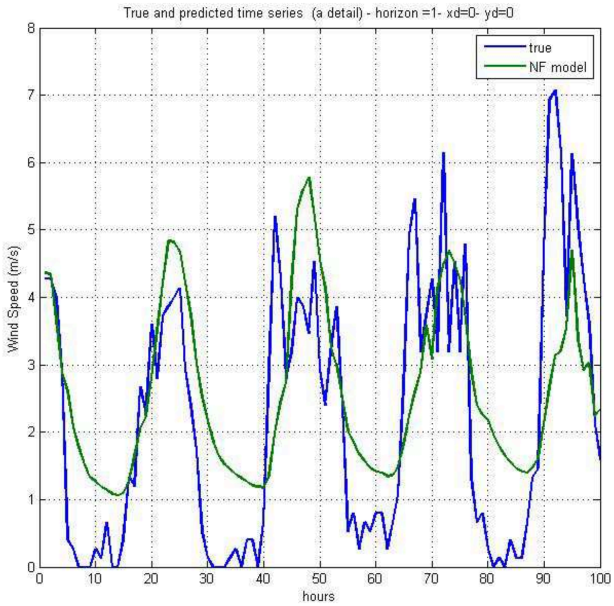

Fig. 6.4. True and predicted hourly average wind speed time series.

number of input variables, I report now the results concerning a NARX Neuro-Fuzzy model, a bit more complex than that described above, represented, with reference to expression (4.2), by $d = q = 2$. The performance of this model, evaluated in terms of *mae* and *rmse* error indices, for prediction horizon in the range $1 \leq h \leq 24$, are reported in Figure (6.5), where the comparison with the persistent model it is also shown. Results indicate that for $1 \leq h \leq 24$ the Neuro-Fuzzy model widely outperform the persistent model. In a nutshell, the maximum value of the *mae* and *rmse* errors are obtained for $h = 10$ and their values are about $1.65 m/s$ and $2.25 m/s$ respectively.

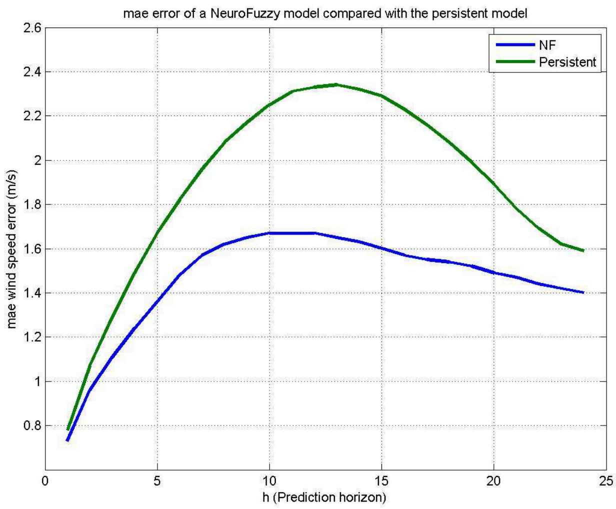

(a)

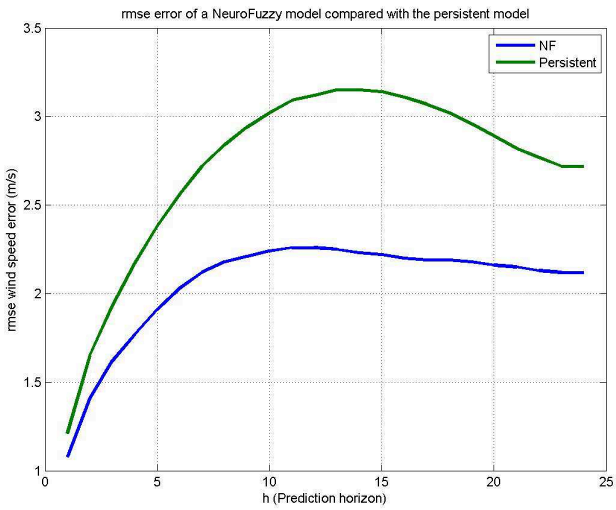

(b)

Fig. 6.5. Performances of the NeuroFuzzy model expressed by (4.2) with $d = q = 2$(a) mae (b) rmse.

6.2 Performances of the ARX and NARX NN approach

In this section I report, as the first result, a comparison among a NARX model obtained by using the sigmoid net approach and a linear version of the auto-regressive model, i.e. an ARX model. Of course the data set and the delays for both the models are the same. In particular, with reference to the general structure (4.2), the model structure is represented by $d = q = 2$. The performances of these two kind of models, in terms of *mae* and *rmse*, are shown in Figure (6.6). In the same Figure, the performance of the persistent model, considered as a low level reference, are reported. As it is possible to see both the NARX and ARX models are significantly more accurate than the persistent model, even at small prediction horizons. This is of course mainly due to the effects of exogenous inputs which are considered for both the ARX and NARX models. Furthermore, Figure (6.6) shows that, as expected, the NARX model encompasses the ARX model.

To conclude this section devoted to models comparison, I report in Figure (6.7) the direct comparison between a Neuro-Fuzzy model and the sigmoid net model with the same degree of complexity ($d = q = 2$). The comparison refer, as usual, the *mae* and *rmse* errors for a range of prediction horizon $1 \leq h \leq 24$. As it is possible to see the sigmoid net model encompasses the corresponding Neuro-Fuzzy model. One reason for the higher accuracy of the sigmoid net model compared to Neuro-Fuzzy model could be found in the different training algorithm considered, but probably the main reason is that the output of the considered Neuro-Fuzzy model is

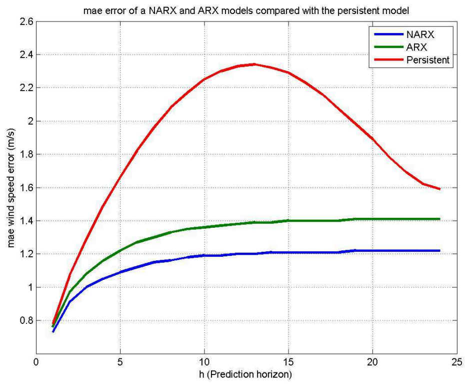

(a)

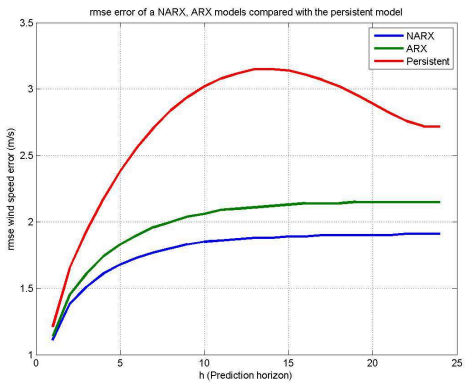

(b)

Fig. 6.6. Comparison among NARX, ARX and Persistent model. The NARX and ARX model have 1 output, (the wind speed), 4 inputs (solar radiation, temperature,Pressure,relative humidity, and $d = q = 2$ (a) mae (b) rmse.

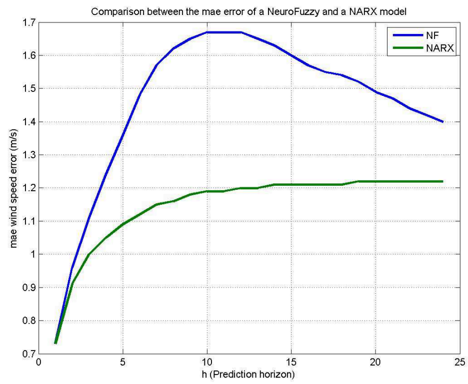

(a)

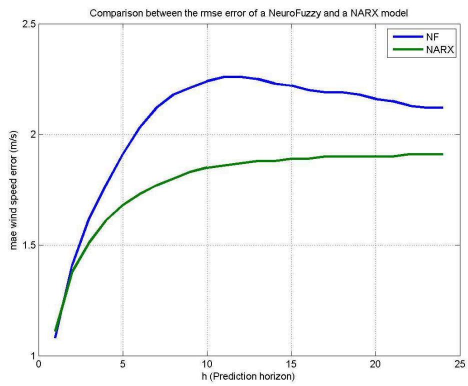

(b)

Fig. 6.7. Comparison between a NeuroFuzzy model and a NARX model with the same complexity ($d = q = 2$) (a) mae (b) rmse.

constrained to be a linear combination of the f arguments. This, on one hand makes easy the model interpretation but, on other hand, decreases the accuracy. The sigmoid net 1-step-ahead prediction model surfaces are reported in Figure (6.8). It is possible to see that, compared with the analogous Neuro-Fuzzy prediction model, these surface are more irregular and also more difficult to be interpreted in terms of simple rules.

6.3 Performances of the EPS approach

In this section results obtained by applying the EPS model structure, identified by using both NF and NN mapping approaches are reported.

6.3.1 Performances of the EPSNF approach

Results obtained by using the NF mapping are reported in Figure (6.9). The Figure shows that among the inter-compared models, the best is the one whose structure is characterized by $d = 12$ and $\tau = 2$. However, for very short prediction horizons (say $h \leq 3$) the model performs almost as the persistent model while for higher prediction horizons significantly outperform persistent model. Furthermore it is possible to observe that the error rate is higher for prediction horizon $h \leq 10$, while for higher horizon the error reach almost a regime value which is about 1.5 m/s in terms of *mae* and 2.3 in terms of *rmse*.

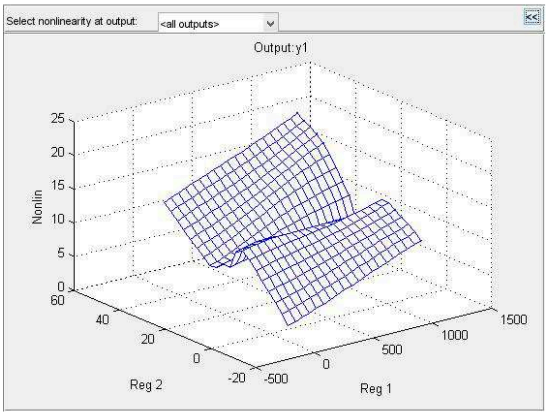

(a)

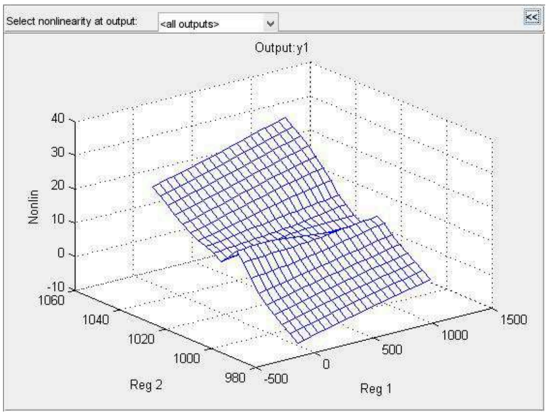

(b)

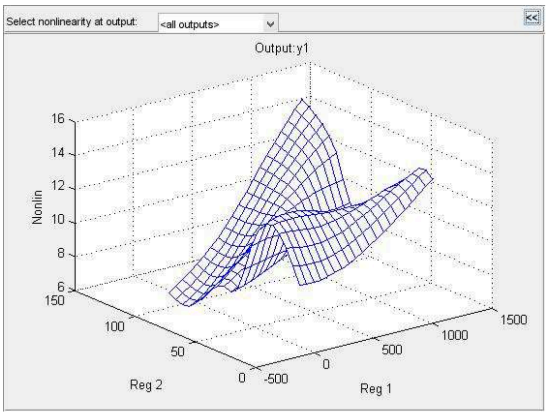

(c)

Fig. 6.8. Surfaces of the 1 step ahead prediction model (a) ws(t+1),sr(t),te(t) (b) ws(t+1),sr(t),pr(t) (c) ws(t+1),sr(t),hum(t).

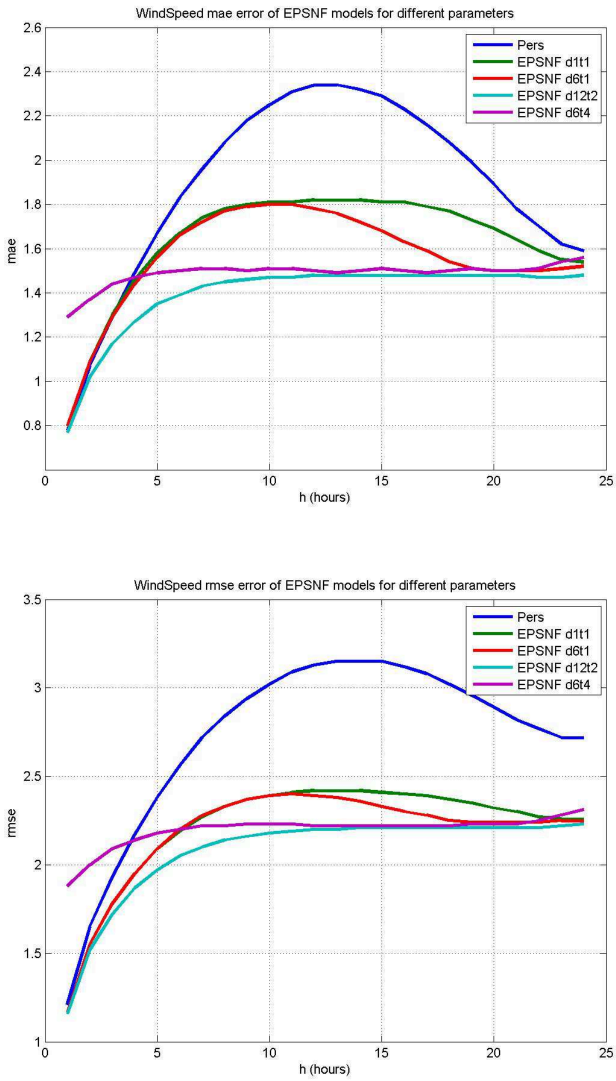

Fig. 6.9. Performances of the EPSNF model for different embedding dimension (a) mae (b) rmse.

6.3.2 Performances of the EPSNN approach

Results obtained by using the NN mapping are reported in Figure (6.10). Roughly speaking to EPSNN model applies similar considerations already expressed for NF models. Indeed, also in this case the best model is the one whose structure is characterized by $d = 12$ and $\tau = 2$. Furthermore the accuracy is almost comparable.

6.4 A direct comparison among NARX and EPS models

Comparing results of all approaches described in this chapter it seems that the NARX ($d = q = 2$) models, whose performance are shown in Figure (6.6, perform slightly better then the EPS models, whose performances are shown in Figure (6.9) and (6.10). This could be explained bearing in mind that the former kinds of models take into account the solar radiation, the air temperature, the atmospheric pressure and the relative humidity, measured at the same station, as exogenous model inputs, while for the latter kinds of models these exogenous were not considered, even, of course, this if this is technically possible.

6.5 Conclusions

The main achievements can be synthesized as follows:

- The accuracy of the studied NARX prediction models, assessed in terms of *mae* and *rmse* is expressed by $mae \leq 1.2m/s$ and

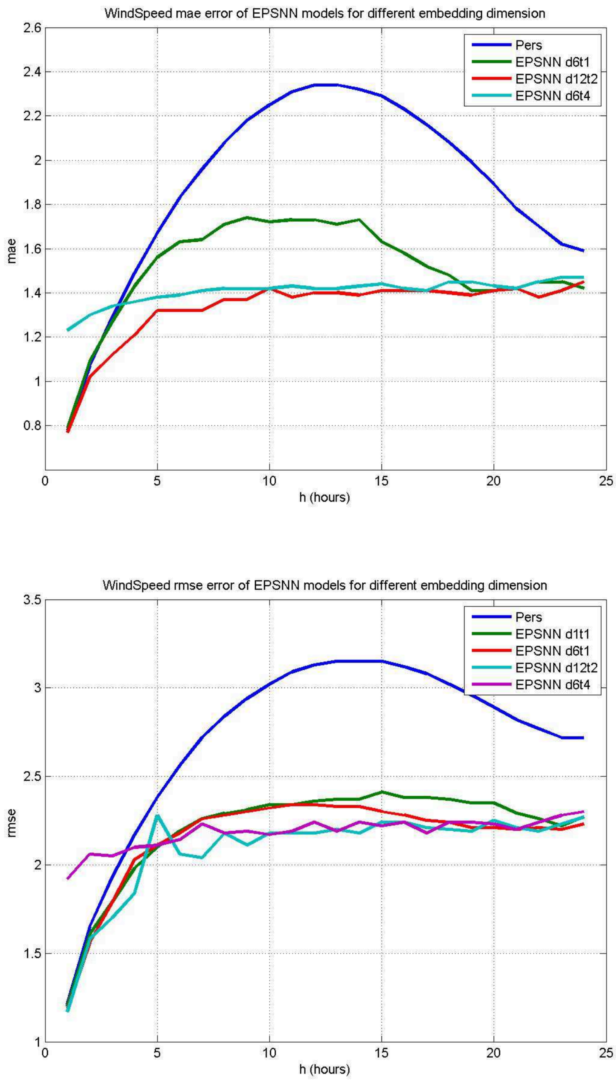

Fig. 6.10. Performances of the EPSNN model for different embedding dimension (a) mae (b) rmse.

$rmse \leq 2.0m/s$, for the whole explored prediction horizon $h \in [1, 24]$.

- for horizons $h \leq 3$ hours the performance of NARX models are $mae \leq 1.0m/s$ and $rmse \leq 1.2m/s$ which can be considered acceptable for applications. Indeed 3 hours ahead reliable predictions can be useful for plant managers to dispatch conventional generators in order to satisfy the electricity demand from the users.

7

Clustering Daily Solar Radiation Time Series

This chapter deals with classification of solar radiation daily patterns into four classes, referred to as clear sky, intermittent clear sky, completely cloud sky and intermittent cloud sky, by using an original features-based classification strategy. The problem is relevant both for analysis and modeling purposes of this kind of time series. Indeed, once classes have been attributed to solar radiation time series, some useful statistics can be carried out, such as computing the permanence in days in each class or computing the weight of each class during a predefined time interval (usually one year). Furthermore, the prediction of some 1-day ahead feature of solar radiation time series can be reformulated in terms of a classification problem. In such a way, instead of predicting 1-day ahead the average value, of solar radiation, the target is that of predicting 1-day ahead the class. To this purpose, an original pair of indices is introduced, referred to as the area ratio A_r and intermittency I. Extraction of these features from solar radiation time series is based on an original strategy, based on the so-called Typical Day, which allows the estimation of the solar radiation that is expected to be measured in a given recording site, avoiding the use of complicate expressions requiring solar altitude, albedo, atmospheric transparency and cloudiness.

7.1 Problem statement

In this chapter it is proposed a new strategy to classify solar radiation daily patterns into to four classes, referred to as clear sky, intermittent clear sky, cloudy sky and intermittent cloudy, as recognized in [50]. An heuristic description of these classes is the following:

- class C_1: the class of clear sky conditions days of solar radiation with very few clouds. An example is reported in Figure (7.1.a).
- class C_2: the class of days characterized by an important solar radiation with some clouds corresponding to a medium level dynamic as shown in Figure (7.1.b).
- class C_3: the class of completely cloudy sky days with big size clouds having a slow speed so that both the intensity of solar radiation and the dynamical level is weak, as shown in Figure(7.1.c).
- class C_4: the class of days with significant sunshine combined with a large number of small clouds with high speed of passages and thus with high dynamic levels. An example is given in Figure (7.1.d).

To discriminate between these four classes may have some drawback. First of all, from the linguistic description given above it is easy to understand that the boundaries between these classes are not clearly distinct since terms as *few clouds*, *some clouds*, *impor-*

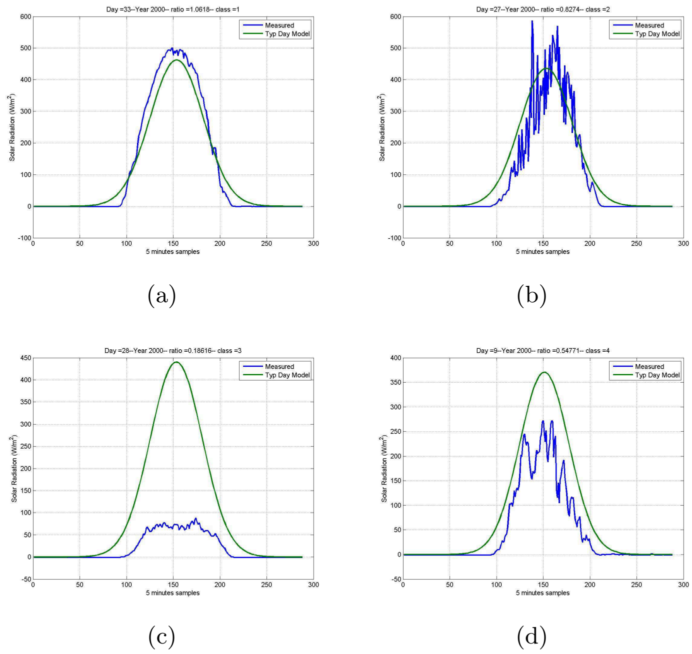

Fig. 7.1. Examples of solar radiation daily patterns (a) class C_1 (b) class C_2 (c) class C_3 (d) class C_4.

tant solar radiation, and so on, which are obvious in natural languages are not so clear when dealing with computing systems. This aspect, which lead Zadeh ([51]) to introduce the concept of fuzzy set, is an indication that boundaries of the described classes are not clear definite. Thus, clustering daily solar radiation patterns it is realistic to expect that each individual pattern may belong to more than on class with different degree of membership. Furthermore patterns of each individual class are time varying, since they exhibits different geometric features (e.g. width and height of the envelop curve) through the year due seasonal effects. As an example in Figure (7.2) class C_1 and C_2 patterns of solar radiation recorded at Aberdeen (Ohio, USA) at different seasons during year 2000 are shown. It is possible to see that despite the pattern shapes are similar, the geometrical features are quite different. In order to overcome this shortcoming, a strategy, based on the Typical Day (TD) model ([52]), was considered to handle the time variance intrinsic with solar radiation data. The aim is to demonstrate that

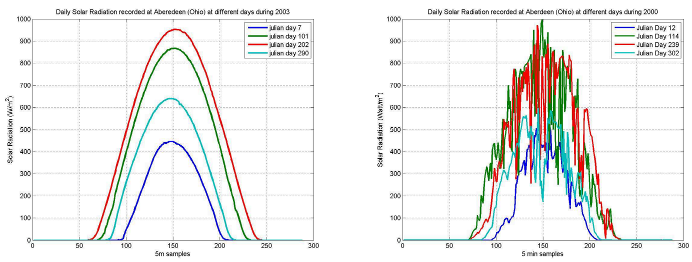

(a) (b)

Fig. 7.2. Solar Radiation Daily patterns recorded at different seasons at the Aberdeen station. (a) class C_1 (b) class C_2.

the four described patterns can be efficiently discriminated by using two indices, referred to as area ratio, A_r and intermittency, I respectively, whose formal description follows.

7.2 The area ratio A_r index

The A_r index is formally represented by expression (7.1)

$$A_r(d) = \frac{A_{pat}(d)}{A_{typ}(d)} \tag{7.1}$$

where $A_{pat}(d)$ and $A_{typ}(d)$ represent the area under the true and the average daily solar radiation pattern at the generic Julian day, d, respectively. In the rest of this chapter, the average daily solar radiation pattern will be referred as $TD(d)$ and thus $A_{typ}(d)$ is the area under $TD(d)$. The procedure to compute $TD(d)$, for simplicity, will be explained in detail in [52]. Of course the A_r index is always positive but can be greater or less than 1. For example, in a day featured by favorable weather conditions (eg. absence of cloud cover and good atmospheric transmittance) A_r will be greater than 1; conversely under thick cloud cover and adverse propagation conditions it may be significantly less than 1. As an example, the behavior of the $A_r(d)$ index computed for solar radiation recorded at Aberdeen during year 2000 is reported in Figure (7.3).

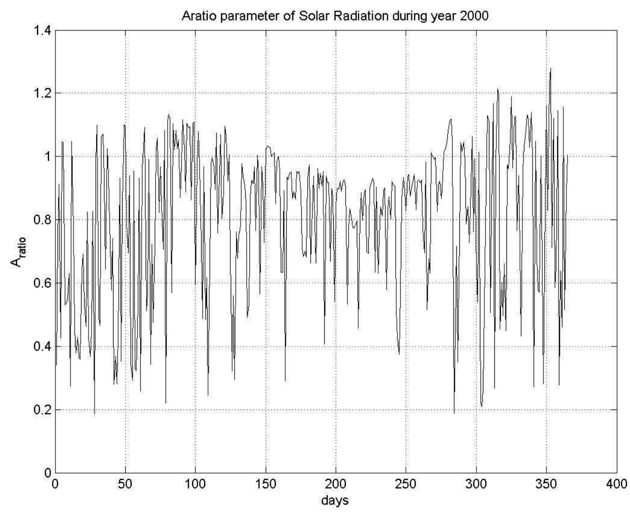

Fig. 7.3. Daily values of the A_r index computed for the Aberdeen station during year 2000

7.3 The *I* index

In order to evaluate the dynamic level which may affect daily solar radiation patterns, it was thought to act as is explained below. The basic observation is that while TD patterns are always represented by smooth bell curves, true daily solar radiation patterns may be featured by a significant intermittency. This certainly occurs for patterns belonging to class C_2 and C_4. For instance in Figure (7.4.a) an example of true daily solar radiation pattern belonging to class C_2 (see the scattered curve) and the corresponding TD pattern (the bell smooth curve) are shown. The power spectral densities corresponding to these two curves are shown in Figure (7.4.b). It is possible to observe that while in the frequency range $[10^0, 10^1]$, corresponding to [1/300, 1/30] Hz, the two spectra are quite similar, they appear significantly different for higher frequencies, say in the range [1/30, 1/3] Hz. In more detail the smooth bell curve, i.e. the TD pattern, exhibits a lower power spectrum density with respect the true pattern. Thus it is reasonable to appropriately consider this feature to point out the presence of intermittency in solar radiation daily patterns. To such a purpose, it is introduced the $I(d)$ index, here referred to as Intermittency, formally expressed by (7.2)

$$I(d) = \frac{\log(Pw_{pat}(d)) - \log(Pw_{typ}(d))}{\log(Pw_{pat}(d)) + \log(Pw_{typ}(d))} \tag{7.2}$$

where $Pw_{pat}(d)$ and $Pw_{typ}(d)$ are the areas under the density power spectrum, in the range [1/30, 1/3] Hz, of the true and TD solar radiation patterns, respectively. To be more clear, with reference at Figure (7.4.b), $I(d)$ is the normalized difference between the log areas under the true and TD curves, respectively, delimited by

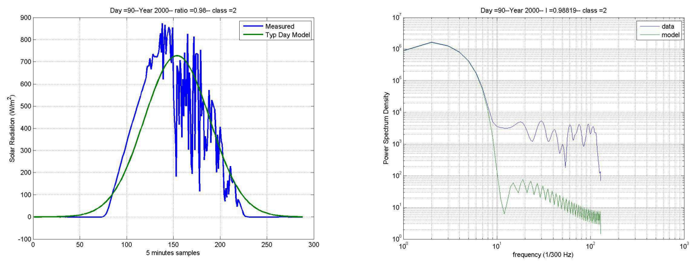

(a) (b)

Fig. 7.4. (a) Example of a true solar radiation daily pattern of class C_2 and corresponding Typical Day (b) Power spectrum densities of the two curves above. The frequency scale is $(5min)^{-1} = 1/300Hz$.

the abscissa 10^1 and 10^2. An example of intermittency computed

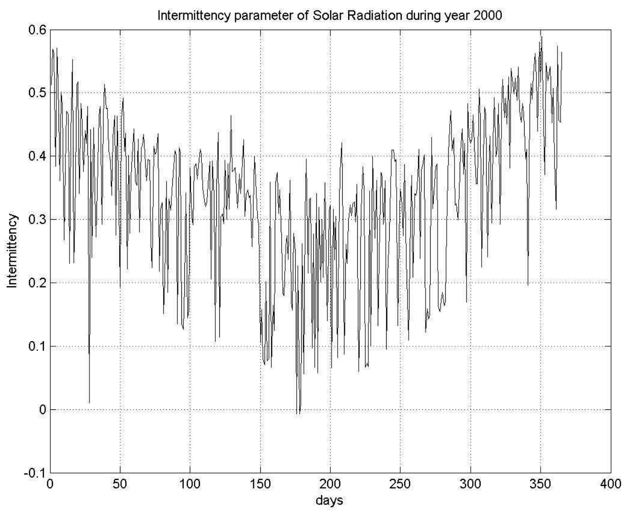

Fig. 7.5. Daily values of the I index computed for the Aberdeen station during year 2000

for the Aberdeen station is shown in Figure (7.5). It can be seen that such a feature takes values in the range $[0, 1]$. In more detail, expression (7.2) shows that when the areas under the spectrum of the true and TD patterns, respectively, are approximately equal, then $I(d) \to 0$, while when the difference of these areas is large, as for instance in the example shown in Figure (7.4.b), then $I(d) \to 1$.

7.4 The proposed classification strategy

In section 7.1 it was conjectured that solar radiation daily patterns can be classified into four classes. The consistency of this hypothesis was preliminary assessed by using an unsupervised learning approach, carried out on 5 min sampled data recorded at the Aberdeen station. To this purpose Self-Organized Maps (SOM) ([53]), implemented in the Matlab © framework have been considered. As it is known, a SOM consists of neurons organized on a regular low-dimensional grid. The SOM can be thought as a network which is spread to space of input data. The network training algorithm moves the SOM weight vectors so that they span across the data such that neighboring neurons on the grid get similar weight vectors. Training a SOM by using solar radiation daily patterns recorded during one year, gives a hits map of the kind shown in Figure (7.6.a). As it is possible to see the SOM neurons can roughly be clustered into four groups, thus confirming the conjecture. The map of the corresponding SOM neighbor weight distances is shown in Figure (7.6.b), which allows to appreciate significant distances among the four groups of neurons.

The feature based classification approach proposed in this work

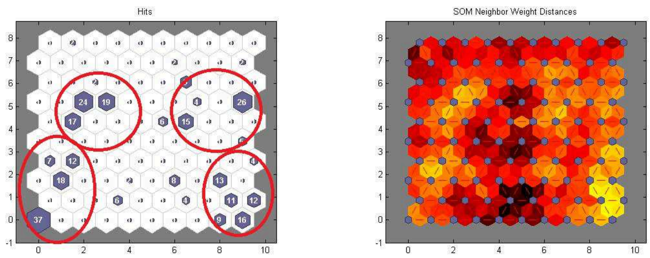

(a) (b)

Fig. 7.6. Unsupervised clustering by using a 10 by 10 Self-Organized Maps (a) SOM hits (b) SOM neighbor weighted distance.

consists of the following two steps:

1. In the first step daily solar radiation patterns are mapped into pairs $(A_r(d), I(d))$ by using expressions (7.1) and (7.2).
2. In the second step the pairs $(A_r(d), I(d))$ are clustered into the four described classes by using the fuzzy c-means (*fcm*) algorithm.

In the next section 7.5 results obtained by using the proposed feature based strategy and the *fcm* clustering approach are reported. Furthermore performances are inter-compared with those obtained by using a neural network classifier trained to work directly with row data.

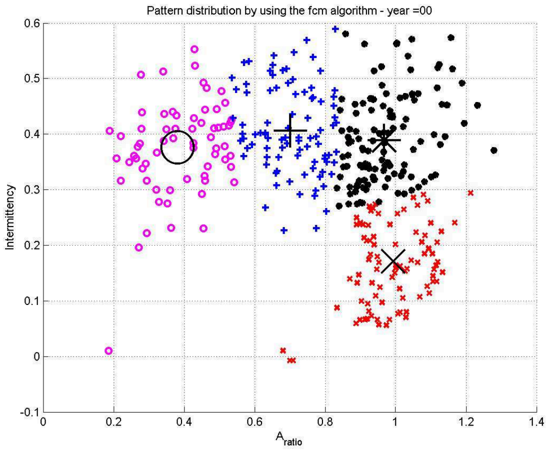

Fig. 7.7. Clusters obtained by using the *fcm* algorithm on data set recorded during year 2000. The centers corresponding to class C_1, C_2, C_3, C_4 are indicated with the symbols $\times$, $*$,$\circ$, and $+$, respectively.

7.5 Numerical Results

The application of the *fcm* algorithm on the features extracted from the Aberdeen solar radiation daily patterns provide the four clusters shown in Figure (7.7). Of course, from this it is not evident to what extent the classification is effective. In order to objectively evaluate the goodness of the proposed features-based classification strategy, it was asked a human expert to classify the raw solar daily radiation patterns, who carried out this task on the basis of the patterns shape, supported, whenever necessary, by other available information such as air temperature, relative humidity, rainfall and wind speed, recorded by the same meteorological station. At the end of the process, it was possible to compute a confusion matrix assuming classes indicated by the human expert as the target classes and classes attributed by the features-based algorithm as output. Such a confusion matrix and the corresponding ROC curves are shown in Figure (7.8). The Figure shows that there is a high agreement be-

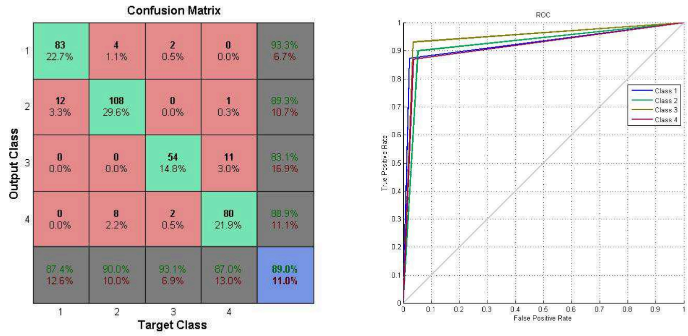

(a) (b)

Fig. 7.8. Performances of the features-based fcm classifier versus the human expert classification (a) Confusion Matrix (b) ROC Curve.

tween the proposed features-based classifier and the human expert classification. In more detail the confusion matrix (Figure (7.8.a)) shows, for instance, that the human expert has indicated a total of 95 patterns as belong to the class C_1. Of these 83 were correctly assigned by the features-based classifier to the class C_1, accounting for 87.4%, while 12, corresponding to the 12.6% have been attributed to the class C_2 and therefore misclassified. Similarly, it is possible to see that of a total of 120 patterns classified by the human expert as belonging to the class C_2 only 4 were classified by the features-based classifier as belonging to the class C_1, and therefore misclassified. This means that the discrimination between patterns of the classes

C_1 and C_2 works quite well. Discrimination between patterns belonging to the classes C_3 and C_4 also works quite well since of a total of 58 pattern classified by the human expert as belonging to class C_3, only 2 were assigned by the features-based classifier to the class C_4 and vice-versa, of a total of 92 pattern assigned by the human expert to the class C_4, only 11 were classified as belonging to the class C_3. A fortiori, the misclassification between classes which are well distinct in the heuristic description, such as C_1 and C_3, is very limited: none of the patterns classified by the human expert as belonging to C_1 were misclassified as belonging to classes C_3 and only 2 patterns assigned by the human expert to class C_3, where classified as belonging to C_1. In overall percentages it is possible to say that 87.4%, 90.0%, 93.1% and 87.0% of events attributed by the human expert to the classes C_1, C_2, C_3 and C_4 respectively have been classified according with the human expert classification. Patterns belonging to class C_3 are those best classified among the four considered classes, as confirmed by the ROC curves shown in Figure (7.8.b). In a very summary, 89% of the total number of solar radiation patterns recorded during the testing year were correctly classified by the proposed features-based classifier.

To further appreciate the convenience of using this classifier, compared with a classifier which works directly with the high dimensional row data, a neural network classifier was trained by using as input the raw high dimensional patterns (each consisting of 288 samples) and as target the four target classes recognized by the human expert. The performance of this classifier are shown in Figure (7.9).

In more detail, from the confusion matrix (Figure (7.9.a)) it is possible to see that the neural network classifier was able to correctly classify about 65.3%, 82.5%, 81.4% and 70.7% of events attributed by the human expert as belonging to the classes C_1, C_2, C_3 and C_4 respectively. Thus, the percentage of patterns correctly classified, compared with the ones shown in Figure (7.8.a), demonstrate that the proposed features-based classifier outperform the neural network classifier operating directly on high dimension row data. This conclusion agrees with [54] who observed that in general, in time series clustering applications, it is not desirable to work directly with raw data. Furthermore, is to be stressed that even for the neural network classifier, class C_3 is that best recognized.

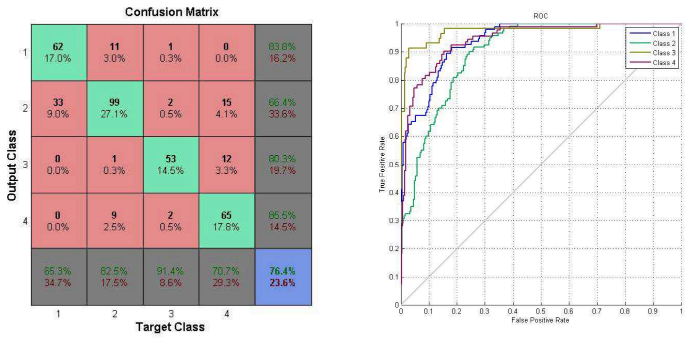

(a) (b)

Fig. 7.9. Performances of a neural network classifier trained by using the original high dimensional solar radiation daily patters and classes recognized by an human expert (a) Confusion Matrix (b) ROC Curves.

7.6 Conclusions

In this work the problem of classify daily solar radiation patterns into four classes by using a features-based classifier, making use of the fuzzy c-means algorithm has been addressed. Results, objectively evaluated in comparison with the classification performed by a human expert, demonstrate that the proposed pair of features allow an effective discrimination among similar classes such as C_1 and C_2 and C_3 and C_4. A fortiori, the misclassification between classes which are well distinct such as C_1 and C_3 is very limited. Furthermore the proposed classifier significantly outperforms a classifier trained to work on raw data, thus justifying the computation effort needed to extract the features. Classification of solar radiation daily patterns is a preliminary step for analysis and modeling purposes of solar radiation time series. Indeed, once daily patterns have been correctly classified, a time series of classes can be associated to the original one, thus allowing the application of alternative analysis and modeling techniques.

8

Clustering Daily Wind Speed Time Series

This chapter deals with the problem of clustering daily wind speed time series based on two features referred to as W_r and H, representing a measure of the relative average wind speed and the Hurst exponent, respectively. Daily values of the pairs (W_r, H) are first classified by means of the fuzzy c-means unsupervised clustering algorithm and then results are used to train a supervised MLP neural network classifier. Further, the problem of predicting 1-step ahead the class of daily wind speed is addressed by introducing NAR sigmoidal neural models into the classification process. The performance of the prediction model is finally assessed. The approach described in this chapter was proposed in [55].

8.1 Introduction

As I have extensively discussed in Chap. 6, hourly average wind speed can be predicted with some accuracy only at very short time horizon. For this reason, the availability of alternative analysis and modeling techniques, such as those that refer to data mining and machine learning, may play a significant role. Indeed to alleviate the problem of predicting future values assumed by a given time series, one might think to associate a series of classes and then trying to predict the class. Of course the prediction problem will be as difficult as higher is the number of considered classes. Time series clustering approaches can be organized into three major categories, depending upon whether they work directly with raw data, indirectly with features extracted from the raw data, or indirectly with models built from the raw data. A survey about time series clustering approaches can be found in [54], while others most recent references can be found in [56]. In the specific field of wind speed time series, some recent papers dealing with application of such a kind of techniques have been proposed for instance by [32], who suggested to classifying wind speed time series according to their intensity and consider the Markov chains for their modeling. Decision trees based on $if - then$ rules, which are one of the most popular methods used in machine learning for classification, have been proposed by [57] with the aim of implementing short term wind speed prediction models. In related renewable energy source fields, such as solar radiation time series, classification of daily time series has been proposed by [50]. Data mining techniques and clustering approaches to classify wind speed data in different cities of Turkey have been adopted by [58].

This chapter proposes to clustering daily wind speed time series based on two features which will be introduced in section 8.2. The data set considered for the present work was taken from the Western Wind Resource Dataset, modeled in the framework of the

Western Wind and Solar Integration Study, freely downloaded from `http://wind.nrel.gov/`.

8.2 Two features of daily wind speed time series

The purpose of this section is to introduce two features of daily wind speed time series, in order to be able to perform their classification. Such features were chosen based on the idea that one of the two indices should represent a normalized measure of the daily average wind speed while the other should represent the correlation properties. The two features, referred to as W_r and H respectively are formally defined as described below.

8.3 The W_r index

As it is known, one of the main features of wind speed is its irregular fluctuating nature which occurs at any time scale [59]. Thus, for instance, 10 m average samples fluctuate with respect to the corresponding hourly average, hourly averages with respect their daily average and, again, daily averages with respect their weekly or monthly averages. As an example, fluctuations of daily average wind speed with respect to the corresponding monthly averages are shown in Figure (8.1). which suggests that the monthly average could be considered, among other possible choices, as a normalizing factor for daily average wind speed. Thus the W_r index, formally defined as in expression (8.1)

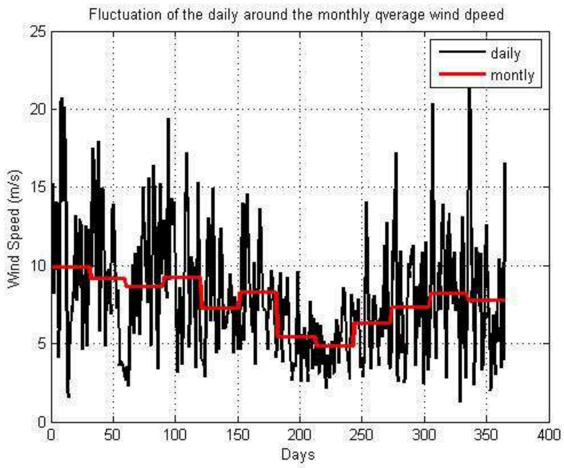

Fig. 8.1. Daily and monthly average wind speed

$$W_r(d) = \frac{\bar{W}(d)}{\bar{W}_m} \qquad d = 1, ..., gg(m), \tag{8.1}$$

where:

- $\bar{W}(d)$ is the daily average wind speed at the generic day d,
- $\bar{W}_m$ is the monthly average wind speed at the month m to which d belongs.
- $gg(m)$ is the number of days in the m_{th} month.

Thus, the W_r index, expresses a relative measure of the daily wind speed intensity. An example of W_r daily time series is shown in Figure (8.2).

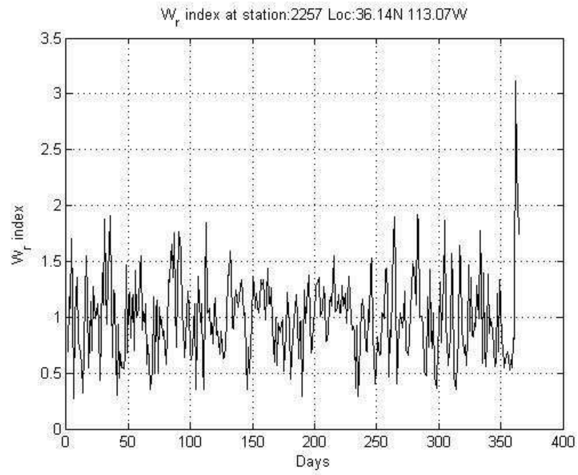

Fig. 8.2. W_r index computed during one year at the station ID2257.

8.4 The Hurst exponent of daily wind speed

In order to represent the correlation properties of daily wind speed time series it was decided to consider the Hurst exponent, H, which can be efficiently computed by several approaches [10]. In particular in this work the Hurst exponent was estimated by using the technique, proposed by Geweke and Porter-Hudak (GPH), as described in the referred paper. The Hurst exponent computed for the average 10-m daily wind speed time series recorded at the station ID2257, which means over time series of 144 values each, is shown in Figure (8.3).

8.5 Wind speed time series classification

The classification approach described in this section consists of the two following steps:

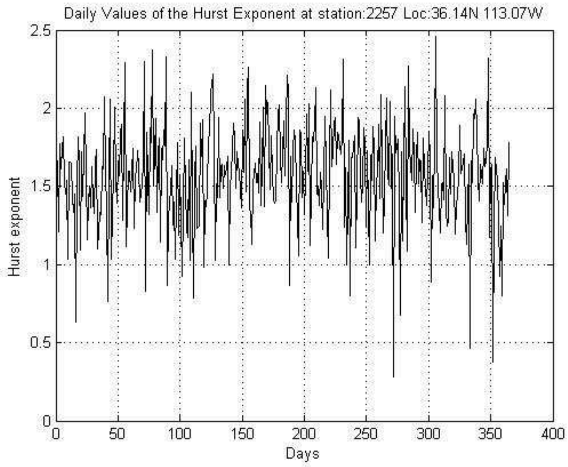

Fig. 8.3. H index computed during one year at the station ID2257.

1. Daily wind speed time series, are mapped into pairs ($W_r(d)$, $H(d)$).
2. The pairs ($W_r(d)$, $H(d)$) are clustered into a pre-defined number of classes by using the fuzzy c-means unsupervised (*fcm*) algorithm [60].

As regarding the choice of the number of classes, a parameter required to run the *fcm* algorithm, classification into two and three clusters have been taken into account, bearing in mind that in view of predicting the class, the problem is as much difficult as higher is the number of considered classes. Clustering examples of ($W_r(d)$, $H(d)$) pairs into 2 and 3 classes are shown in Figure (8.4). As it is possible to see, when clustering into 2 classes (see Figure (8.4.a)), patterns essentially distributed following the W_r index, which thus plays the role of dominant feature. Roughly speaking it is possible to say that in a 2-class framework, class C_1 is represented by

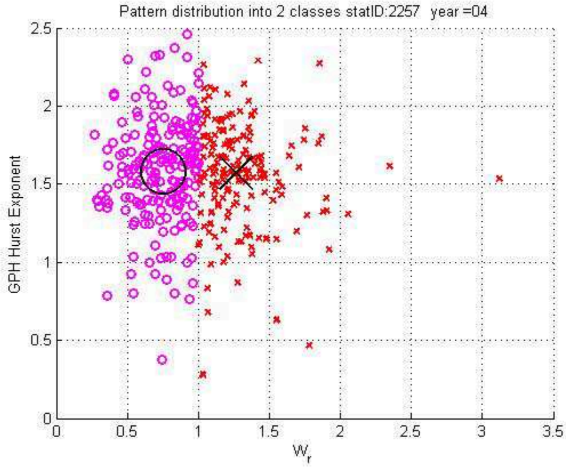

(a) 2 classes

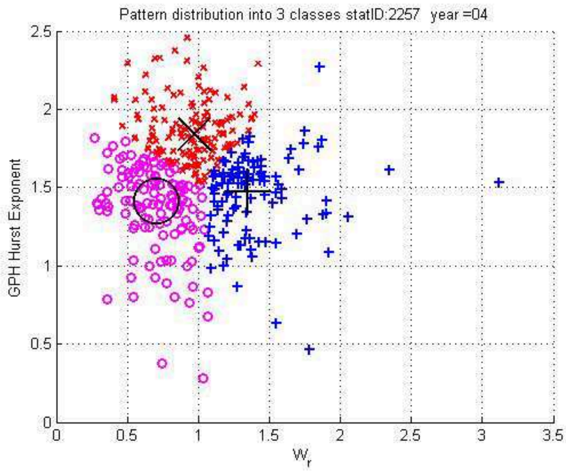

(b) 3 classes

Fig. 8.4. *fcm* classification of daily wind speed time series.

daily patterns featured by $W_r \leq 1$, while, of course, class C_2 by $W_r > 1$. For the 3-class framework (see Figure (8.4.b)), the *fcm* algorithm takes into account the H index. Roughly speaking in this framework, class C_1 is featured by $W_r \leq 1$, class C_3 is featured by $W_r > 1$ and $H < 2$ while the remaining patterns belong to class C_2. For practical reasons, in this work, once a representative set of patterns was classified by using the unsupervised *fcm* algorithm, a supervised MLP classifier was trained to classify new incoming patterns.

8.6 Some applications

Once classes have been attributed to daily wind speed time series, some useful statistics can be carried out, such as computing the permanence in days in each class or computing the weight of each class during a predefined time interval (usually one year). For instance, Figure (8.5.a) shows that at the station ID2255, during 2004, about 130 daily patterns persists at least 2 days in class C_1, but less than 20 persist at least 5 days. Similarly, from Figure (8.5.b) it is possible to see that in a 3-class framework about 50 patterns persist in class C_3 at least 2 days, but less than 20 persist at least 3 days. It is trivial to observe that indicating as $n_i(p)$ the number of patterns in a year that persist at least p days and as n_c the number of classes, it is possible to compute the weight of each class W_i as indicated in expression (8.2).

$$W_i\% = \frac{n_i(1)}{\sum_{i=1}^{n_c} n_i(1)} 100 \tag{8.2}$$

Thus, for instance, evaluating from Figure (8.5.a) that $n_1(1) = 195$ and $n_2(1) = 170$ the weight of class C_1 and C_2 at the station ID2257, in a 2-class framework are $W_1\% = 53$ and $W_1\% = 47$, respectively.

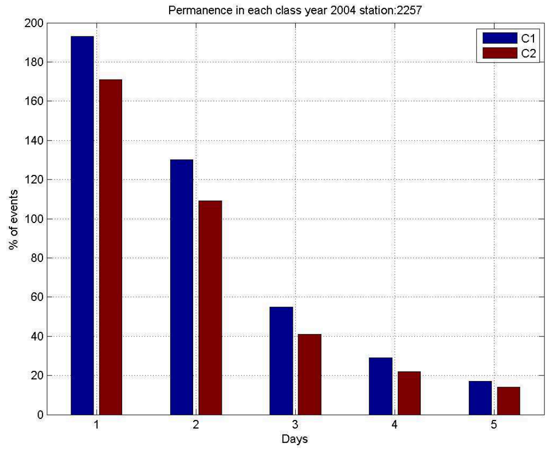

(a)

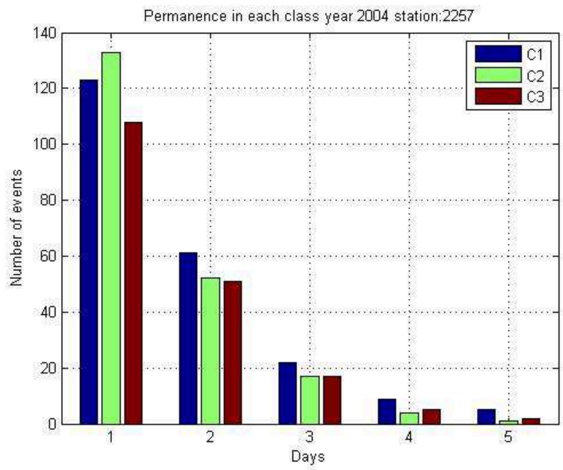

(b)

Fig. 8.5. Permanence (in days) in the same class at the station ID2257. (a) 2-class framework (b) 3-class framework

8.7 Predicting the class

In this section the problem of predicting 1-day ahead the class of daily wind speed time series, will be addressed. The strategy consists of the following two steps:

1. identify prediction models for $W_r(d)$ and $H(d)$, in order to compute the corresponding predicted pairs ($\hat{W}_r(d)$ and $\hat{H}(d)$),
2. use a supervised classifier to associate a class to the predicted pairs ($\hat{W}_r(d)$, $\hat{H}(d)$).

8.8 Identify $\boldsymbol{NAR}$ models for $\boldsymbol{W_r(d)}$ and $\boldsymbol{H(d)}$

Dealing with step 1, NAR models, expressed by 4.1, were taken into account. Of course, in the considered application the discrete time t is evaluated in days while the model oreder d was evaluated by using the mutual information, as shown in Figure (8.6). As it is possible to see the mutual information of the individual $W_r(d)$ and $H(d)$ time series decays very sharply, reaching the lowest level, for the first time, after 2 or 3 lags. Based on this result the number of considered delays for the considered NAR model (4.1) can be set equal to 2 or 3. Nevertheless, in this work, trials were carried out also by considering a larger number of delays. As concerning the problem of estimating the non-linear function f in expression (4.1), sigmoidal neural networks were considered, for all trials shown in this work. The number of sigmoid was heuristically set, after some trials, on the order of 15. The available data set was divided, as usual in good practice, into a training and a testing data set, in order to avoid polarization of the identified models.

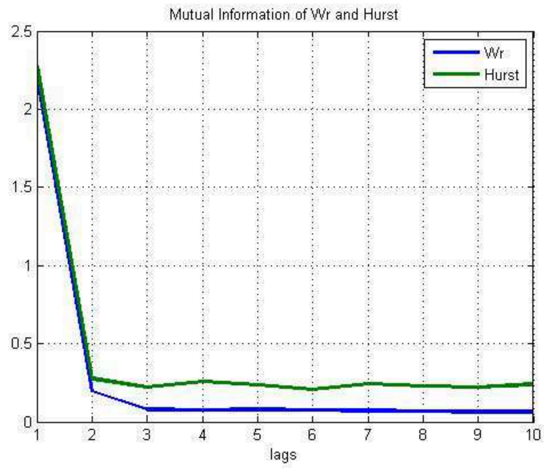

Fig. 8.6. Mutual Information of W_r and H daily values, respectively.

The time behavior of two independent 1-step ahead neural networks based NAR models, to predict W_r and H daily values, respectively, are shown in Figure (8.7). However, it is to bearing in mind that in the considered application, the predicted pairs $\hat{W}_r(d)$ and $\hat{H}(d)$ are not the final target, since they are the input for a MLP classifier, which was appropriately trained to associate a class to each predicted pair. Thus, in the final instance, the model evaluation must be performed by comparing the class assigned by the fcm classifier (assumed as target) to the ($W_r(d)$,$H(d)$) pairs, computed directly from true time series, and that assigned by the MLP classifier to the corresponding predicted ($\hat{W}_r(d)$,$\hat{H}(d)$) pairs. A strategy to objectively perform such a comparison and results obtained are described in the next section 8.9.

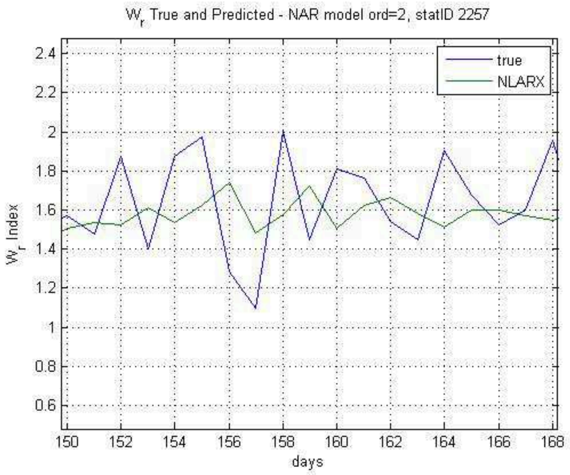

(a) Wr daily values

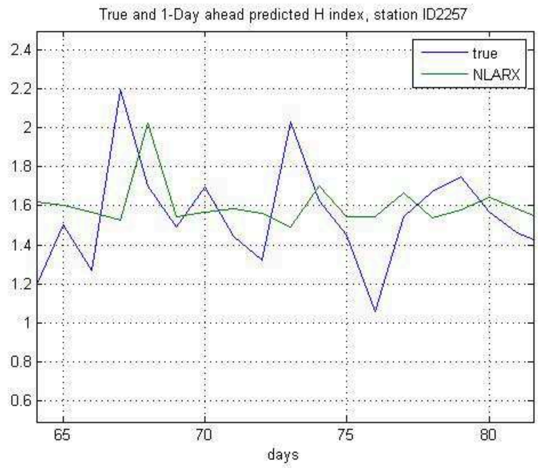

(b) H daily values

Fig. 8.7. 1-step ahead prediction of W_r and H by using a NAR model.

8.9 Assessing the performance

The problem of objectively compare a true and a predicted time series of classes can be performed in several ways. In this work performance was assessed in terms of True Positive Rate (TPR), True Negative Rate (TNR), and Confusion Rate (CR). In simple terms,

- the True Positive Rate (TPR), is the pattern proportion in a given class which are correctly classified,
- the True Negative Rate (TNR), is the proportion of patterns which are correctly identified as not belonging to a given class.
- the Confusion Rate (CR), is the fraction of samples misclassified, considering the overall number of class.

In literature the TPR and the TNR are also referred to as Sensitivity and Specificity, so these terms will be interchangeable used in the rest of this work. It is worth nothing that a good predictor would be characterized by values of Sensitivity and Specificity both close to 1, while small values of CR (close to zero) are best. For the 2-class framework, the TPR and CR indices computed for the station ID2257 by using NAR models, with model order in the range $d \in [2, 30]$, are shown in Figure (8.8). The TNR rate is not reported since for a 2-class framework relations (8.3) hold

$$\begin{aligned} TNR(1) =& TPR(2) \\ TNR(2) =& TPR(1) \end{aligned} \tag{8.3}$$

where the integer number in brackets represents the class. The horizontal lines in Figure (8.8) refer to the TPR, and CR indices computed for the persistent model which, of course, are not affected by

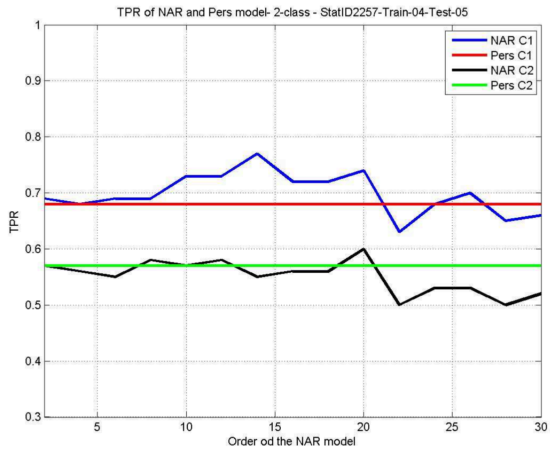

(a)

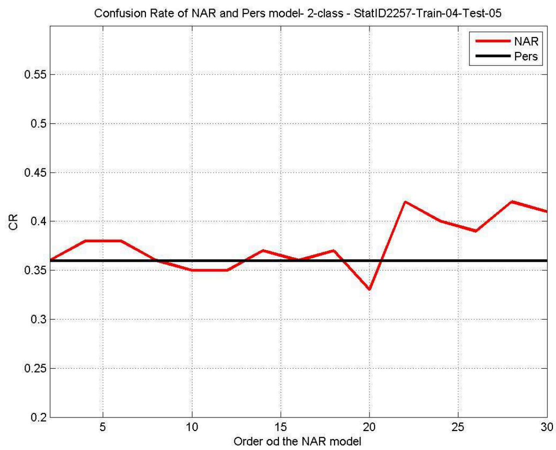

(b)

Fig. 8.8. TPR and CR for the station 2257 computed by NAR models with order ranging from 2 to 30(a) TPR (b) CR

the model order d. Figure (8.8.a) shows that for the 2-class framework it is always $TPR(1) \geq 0.7$ and $TPR(2) \geq 0.5$, respectively. Furthermore it seems that the TPR(1) could improve, reaching a maximum close to 0.8, for model order of about $d = 13$, but unfortunately an equivalent improvement is not observed for the TPR(2) index, which slightly oscillates around the value 0.57. The overall performance are well represented by the CR rate (see Figure (8.8.b)) which seems to oscillate around the level of 0.36, obtained for $d = 2$. This is also the level reached by the persistent model. Thus, as expected, there is not a real convenience, in terms of model performance, in choosing NAR models of order higher than $d = 2$. Furthermore, it is possible to conclude that there is non any convenience in using a NAR models with respect to the simple persistent model. Indeed for $d = 2$ the two kinds of models exhibits almost identical performances. Nevertheless, results show that 1-day ahead prediction of the wind speed class could be helpful, in a 2-class framework, since the overall confusion rate is about 0.36.

The performances for the 3-class framework obtained for station ID2257 are reported in Figure (8.9). In short, it seems that $0.3 \leq TPR \leq 0.5$ and $0.6 \leq TNR \leq 0.8$ for all classes, resulting in a Confusion Rate (see Figure (8.9.c) larger than 0.6 for all NAR model orders. Furthermore, in this framework, the persistent model slightly outperform the NAR model since exhibits a level of CR of about 0.54. However, it is possible to conclude that in a 3-class framework, 1-day ahead of wind speed class prediction is not reliable nor with the NAR model nor with the persistent model.

In order to see, if conclusions reached for the station ID2257 can be extended, the data set of 3 others stations, referred to as ID2300,

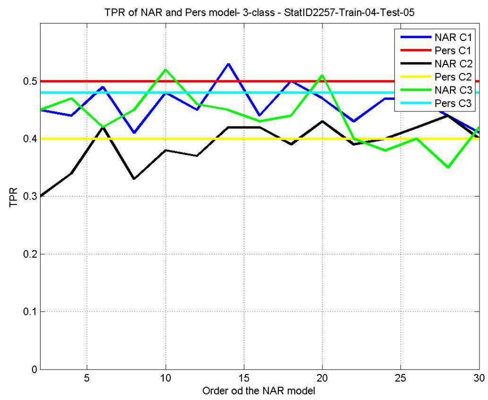

(a)

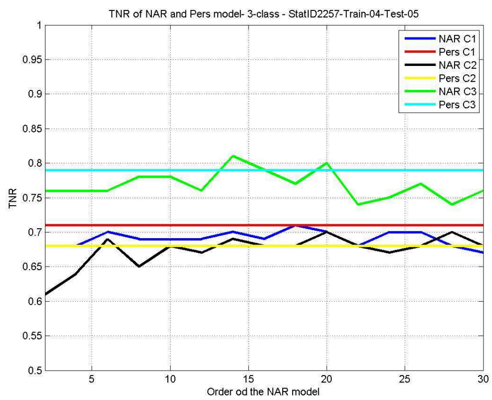

(b)

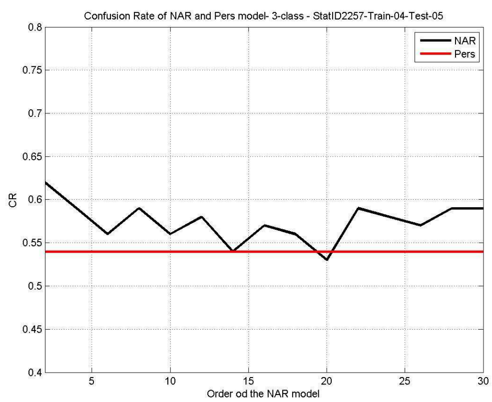

(c)

Fig. 8.9. Sensitivity and Specificity rates for station 3357 for model order ranging from 2 to 30 (a) TPR (b) TNR (c) CR

ID6435 and ID9400 are reported in this work. The peculiarity of stations ID6435 and ID9400of with respect to stations ID2257 and ID2300 is that they are installed at 1782 m and 2201 m above sea level, respectively, while station ID2257 and ID2300 are offshore. For simplicity, here only the CR are (see Figure (8.10) and limited to the 2-class framework. Results shows that, in the 2-class frame-

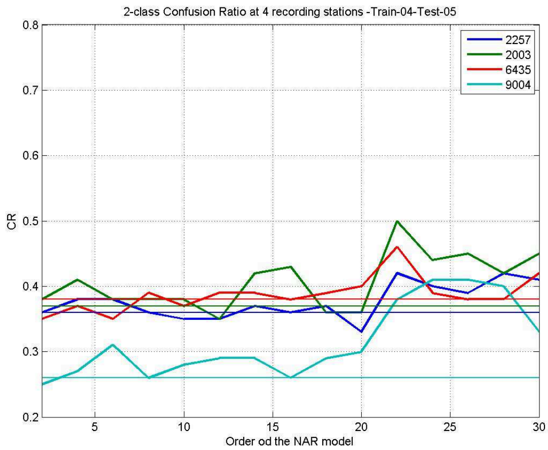

Fig. 8.10. Confusion rate at different recording stations.

work, the overall CR is better than 0.38, for all considered stations, provided to use NAR low order models (i.e. $d = 2$). However, similar performances could be obtained also by using the simple persistent model.

8.10 Conclusions

In this chapter, a feature based strategy to classify daily wind speed time series, based on a couple of indices referred to as W_r and H, has been proposed. The classification allows to compute some useful statistical property such as the permanence of patterns in a given class. The problem of predicting 1-step ahead the class of daily wind speed time series has also been addressed by using NAR neural network models, with sigmoidal activation functions. Results shows that limited to a 2-class framework, there could be some benefit in using the proposed 1-day ahead class prediction model. Nevertheless, in principle, the 1-day ahead prediction of the wind speed class by means of NAR models does not provide outstanding results, CR being a little lower than the 40% only for the classification into two classes. However, it must be said that others approaches are possible to perform the class prediction, that were not taken into account in this work and could represent one of the future development of the Thesis.

9

Concluding remarks

In this work the problem of analyze and model solar radiation and wind speed time series was addressed. This issues, as well as being a fascinating research topic, may have practical consequences in the problem of prediction in the short term, which is of great interest for managers of power plants. The studied prediction models, in agreement with the initial choice, are based on information that can be gathered from time series recorded at the site of interest only, thus excluding in the modeling process any other information, including the fact that, as discussed in Chap. 1, the processes involved are spatial distributed. This radical choice of field was carried out since the main aim of the studied prediction models, is that of being agile, in contrast with the prediction models of type NWP (Numerical Weather Prediction), which are undoubtedly more accurate, but complex and thus not appropriate for several reasons. On the other hand a huge effort has been devoted in literature to prediction models based on time series only. Although such a considerable interest, it seems that contours of the considered prediction problems are not fully understood

and often the authors consider that processes underlying solar radiation and wind speed as simply not linear.
For this reason, the first part of this Thesis was devoted to perform a deeply analysis of solar radiation and wind speed time series, not limited to the traditional stationary, spectral and autocorrelation analysis. Indeed analysis carried out in chapters 2 and 3, was addressed to clarify several concerns of considered time series, including the hypothesis that the considered processes could be chaotic. However, the interpretation of chaos analysis results is at the present controversial. Indeed, unless analysis point out the presence of positive Lyapunov exponents, in both wind speed and solar radiation time series, it was not possible to determine a reasonable low dimension for the supposed chaotic attractors. A better understanding of these issues could lead to better prediction results than those presented in this work. Nevertheless, the modeling technique adopted (i.e. the Embedding Phase Space representation) is the one most widely used for modeling of complex systems and therefore considered appropriate for the purposes of this work. Furthermore identification of model parameters was performed with both Neuro-Fuzzy and Artificial Neural Networks which are among the most powerful nonlinear identification techniques available. The modeling work allowed the estimation, on an experimental basis, of bounds for the prediction error, in terms of *mae* and *rmse*, in the whole explored horizon. In a nutshell (see Chapters 5 and 6 for details) it can be said that while the proposed models are effective for the prediction of solar radiation throughout the time horizon explored $h \in [1, 24]$, are less effective for the prediction of wind speed. Indeed for wind

speed the studied models are reliable for short time horizon (3 to 5 hours), only. Furthermore in this case their performance slightly outperforms the simple persistent model.
Another result of this work is the formulation of the prediction problem, at daily scale, in terms of class prediction which provides new modeling opportunities, that at the present are almost unexplored. Indeed in the Thesis only classification with the *fcm* algorithm and class prediction by using NAR models was carried out, leaving unexplored a plethora of techniques, which currently are referred to as *machine learning* techniques, which may provide some further benefits. To explore more deeply these new opportunities could be another intriguing future developments of this work.
As mentioned above, the major limitations of the work carried out was undoubtedly that the modeling was performed by considering time series recorded at individual recording stations, while the physical processes underling the formation of wind speed and solar radiation are distributed processes. This limitation is often not overcoming for the lack of recording stations in a given area. However, nowadays since large distributed plants are available, it could be taken in to account the possibility to involve, in the modeling process, correlation among time series recorded at different stations. To explore these aspects is leaved as another of the future developments of the undertaken research.

10

Acknowledgements

I wish to thank very much my tutors Prof. Luigi Fortuna and Professor Giorgio Guariso for several tips and encouragement during this work. I wish also to thank my parent's and friends for their invaluable encouragement.

References

1. AAVV, Photovoltaic plants, ABB Technical Application Paper N. 10 1–124.
2. AAVV, Wind power plants, ABB Technical Application Paper N. 13 1–136.
3. S. Kaplanis, E. Kaplani, A model to predict expected mean and stochastic hourly global solar radiation values, Renewable Energy 32 32 (2007) 1414–1425.
4. A. Maafi, S. Harrouni, Preliminary results of the fractal classification of daily solar irradiance, Solar Energy 75 (2003) 53–61.
5. S. Harrouni, A. Guessoum, Using fractal dimension to quantify long-range persistence in global solar radiation, Chaos, Solitons and Fractal 41 (2009) 1520–1530.
6. Z. Zeng, H. Yang, R. Zhao, J. Meng, Nonlinear characteristics of observed solar radiation data, Solar Energy 87 (2013) 204–218.
7. T. Feng, Z. Fu, X. Deng, J. Mao, A brief description to different multi-fractal behaviors of daily wind speed records over china, Physics Letters A 373 (2009) 41344141.
8. T. E. Karakasidis, A. Charakopoulos, Detection of low-dimensional chaos in wind time series, Chaos, Solitons and Fractals 41 (2009) 1723–1732. doi:10.1016/j.chaos.2008.07.020.
9. L. Fortuna, S. Nunnari, G. Guariso, Fractal order evidences in wind speed time series, in: Proceedings of 2014 International Conference on Fractional Differentiation and its Applications, pp. 1–6. doi:10.1109/ICDFA.2014.6967450.
10. R. Weron, Estimating long range dependence finite sample properties and confidence intervals, Physica A 312 (2002) 285–299.
11. R. Hegger, H. Kantz, T. Schreiber, Practical implementation of nonlinear time series methods: The tisean package, Chaos 9 (1999) 413–435.

12. A. Costa, A. Crespo, J. Navarro, G. Lizcano, H. Madsend, E. Feitosa, A review on the young history of the wind power short-term prediction, Renewable and Sustainable Energy Reviews 12 (2008) 1725–1744.
13. J. Carta, P. Ramirez, S. Velazquez, A review of wind speed probability distributions used in wind energy analysis - case studies in the canary islands, Renewable and Sustainable Energy Reviews 13 (2009) 933–955.
14. C. Monteiro, R. Bessa, V. Miranda, A. Botterud, J. Wang, G. Conzelmann, Wind power forecasting: State-of-the-art 2009, Argonne National Laboratory.
URL `http://www.osti.gov/bridge`
15. M. Lei, L. Shiyan, J. Chuanwen, Z. Y. L. Hongling, A review on the forecasting of wind speed and generated power, Renewable and Sustainable Energy Reviews 13 (2009) 915–929.
16. X. Zhao, S. Wang, T. Li, Review of evaluation criteria and main methods of wind power forecasting, Energy Procedia 12 (2011) 761–769.
17. G. Giebel, R. Brownsword, G. Kariniotakis, M. Denhard, C. Draxl, The state of the art in short-term prediction of wind power - a literature overview, Project ANEMOS Deliverable Report D1.1, 2003http://www.anemos-plus.eu/ (2011) 1–110.
18. E. Bossanyi, Short-term wind prediction using kalman filters, Wind Engineering 9(1) (1985) 1–8.
19. L. Kamal, Y. Z. Jafri, Time series models to simulate and forecast hourly averaged wind speed in quetta, pakistan, Solar Energy 61 (1991) 23–32.
20. J. L. Torres, A. Garcia, M. D. Blas, A. DeFrancisco, Forecast of hourly average wind speed with arma models in navarre (spain), Solar Energy 79 (2005) 65–77.
21. E. Erdem, J. Shi, Arma based approaches for forecasting the tuple of wind speed and direction, Applied Energy 88 (2011) 1405–1414.
22. H. Liu, E. Erdem, J. Shi, Comprehensive evaluation of arma-garch(-m) approaches for modeling the mean and volatility of wind speed, Applied Energy 88 (2011) 724–732.
23. E. Cadenas, W. Rivera, Wind speed forecasting in three different regions of mexico, using a hybrid arima - ann model, Renewable Energy 35 (2010) 2732–2738.
24. S. Nunnari., L. Fortuna, A. Gallo, Wind time series modeling for power turbine forecasting, International Journal of Electrical Energy 2 (2014) 112–118. `doi:10.12720/ijoee.2.2.112-118`.
URL `http://dx.medra.org/10.12720/ijoee.2.2.112-118`
25. J. Wu, C. K. Chan, Prediction of hourly solar radiation using a novel hybrid model of arma and tdnn, Solar Energy 85 (2011) 808–817.

26. G. Li, J. Shi, On comparing three artificial neural networks for wind speed forecasting, Applied Energy 87 (2010) 2313–2320.
27. Z. Guo, W. Zhao, H. Lu, J. Wang, Multi-step forecasting for wind speed using a modified emd-based artificial neural network model, Renewable Energy 37 (2012) 241–249.
28. O. B. Shukur, M. H. Lee, Daily wind speed forecasting through hybrid kf-ann model based on arima, Renewable Energy 76 (2015) 637–647.
29. A. U. Haque, P. Mandal, M. E. Kaye, J. Meng, L.Chang, T. Senjyu, A new strategy for predicting short-term windspeed using soft computing models, Renewable and Sustainable Energy Reviews 16 (2012) 4533–4573.
30. M. Mohandes, S. Rehman, S. Rahman, Estimation of wind speed profile using adaptive neuro-fuzzy inference system (anfis), Applied Energy 88 (2011) 4024–4032.
31. G. C. M. Beccali and, A. Marvuglia, C. Serporta, Estimation of wind velocity over a complex terrain using the generalized mapping regressor, Applied Energy 87 (2010) 884–893.
32. Z. Song, X. Geng, A. Kusiak, C. Xu, Mining markov chain transition matrix from wind speed time series data, Expert Systems with Applications 38 (2011) 10229–10239.
33. L. Han, C. E. Romero, Z. Yao, Wind power forecasting based on principle component phase space reconstruction, Renewable Energy 81 (2015) 737–744.
34. H. Bouzgou, N. Benoudijt, Multiple architecture system for wind speed prediction, Applied Energy 88 (2011) 2463–2471.
35. M. C. Alexiadis, P. S. Dokopoulos, H. S. Sahsamanoglou, Wind speed and power forecasting based on spatial correlation models, IEE Transactions on Energy Conversion 14 (1999) 836–842.
36. H. Sun, D. Yan, N. Zhao, J. Zhou, Empirical investigation on modeling solar radiation series with armagarch models, Energy Conversion and Management 92 (2015) 385–395.
37. J. Wu, C. K. Chan, Prediction of hourly solar radiation using a novel hybrid model of arma and tdnn, Solar Energy 85 (2011) 808–817.
38. A. M. A. Baig, P-Achter, Prediction of hourly solar radiation using a novel hybrid model of arma and tdnn, Solar Energy 1 (1991) 119–123.
39. Z. Nian, P. Behera, Solar radiation prediction based on recurrent neural networks trained by levenberg-marquardt backpropagation learning algorithm, Innovative Smart Grid Technologies (ISGT), 2012 IEEE PES (2012) 1–7doi:10.1109/ISGT.2012.6175757.

40. A. Yona, T. Senjyu, T. Funabashi, C. Kim, Determination method of insolation prediction with fuzzy and applying neural network for long-term ahead pv power output correction, IEEE Transactions on Sustainable Energy 4 (2013) 527–533.
41. J. Piri, O. Kisi, Modelling solar radiation reached to the earth using anfis, nn-arx, and empirical models (case studies: Zahedan and bojnurd stations), Journal of Atmospheric and Solar-Terrestrial Physics 123 (2015) 39–47.
42. V. Prema, K. U. Rao, Development of statistical time series models for solar power prediction, Renewable Energy 83 (2015) 100–109.
43. W. Yao, Z. Li, T. Xiu, Y. Lu, X. Li, New decomposition models to estimate hourly global solar radiation from the daily value, Solar Energy 120 (2015) 87–99.
44. O. Kisi, Modeling solar radiation of mediterranean region in turkey by using fuzzy genetic approach, Energy Conversion and Management 64 (2014) 429–436.
45. P. Alvanitopoulos, I. Andreadis, N. Georgoulas, M. Zervakis, N. Nikolaidis, Solar radiation prediction model based on empirical mode decomposition 2014 IEEE International Conference on Imaging Systems and Techniques (IST) (2014) 161–166. doi:10.1109/IST.2014.6958466.
46. P. Lauret, J. Boland, B. Ridley, Bayesian statistical analysis applied to solar radiation modelling, Renewable Energy 49 (2013) 124–127.
47. S. Navin, S. Pranshu, I. David, S. Prashant, Predicting solar generation from weather forecasts using machine learning, IEEE International Conference on Smart Grid Communications (Smart Grid Comm),Brussels, Belgium.
48. Z. Nian, P. Behera, C. Williams, Solar radiation prediction based on particle swarm optimization and evolutionary algorithm using recurrent neural networks, IEEE International Systems Conference (SysCon) 2013 (2013) 280–286doi:10.1109/SysCon.2013.6549894.
49. T. Takagi, M. Sugeno, Fuzzy identification of systems and its applications to modeling and control, IEEE Trans. on Systems, Man, and Cybernetics 1 (1985) 116–132.
50. T. Soubdhan, R. Emilion, R. Calif, Classification of daily solar radiation distributions using a mixture of dirichlet distributions, Solar Energy 83 (2009) 1056–1063. doi:10.1016/j.chaos.2008.07.020.
51. L. A. Zadeh, Fuzzy sets, Information and Control 8 (1965) 338–353.
52. L. Fortuna, S. Nunnari, A. Gallo, A typical day based approach to detrend solar radiation time series, in: Proceedings of the 3rd ACM International Regular and Data Challange Workshop on Multimedia Analysis for Ecological Data (MAED'14) November 07 2014,, Sheridan Printing, Orlando, FL – USA, pp. 1–6. doi:http://dx.doi.org/10.1145/2661821.2661823.

53. T. Kohonen, Self-Organizing Maps, 1995.
54. T. W. Liao, Clustering of time series data - a survey, Pattern Recognition 38 (2005) 1857–874.
55. L. Fortuna, G. Guariso, S. Nunnari, One day ahead prediction of wind speed class, in: Proceedings of the 4th International Conference on Renewable Energy Research and Applications, Palermo, Italy, pp. 1–6.
56. S. Rani, G. Sikka, Recent techniques of clustering of time series data: A survey, International Journal of Computer Applications 52 (2012) 1–9.
57. A. Troncoso, S. Salcedo-Sanz, C. Casanova-Mateo, J. R., L. Prieto, Local models-based regression trees for very short-term wind speed prediction, Renewable Energy 81 (2015) 589–598.
58. S. I. Colak and, M. Demirtas, M. Yesilbudak, A data mining approach: Analyzing wind speed and insolation period data in turkey for installations of wind and solar power plants, Energy Conversion and Management 65 (2013) 185–197.
59. T. Laubrich, H. Kantz, Statistical analysis and stochastic modelling of boundary layer wind speed, Eur. Phys. J. Special Topics 174 (2009) 197–206.
60. J. Bezdek, R. Ehrlich, W.Full, fcm: the fuzzy c-meams clustering algorithm, Computers & Geosciences 10 (1984) 191–203.